



**HAL**  
open science

# Influence of High-Frequency Operation on the Efficiency of a PMSM Drive with SiC-MOSFET Inverter

Paisak Poolphaka, Ehsan Jamshidpour, Thierry Lubin, Lotfi Baghli,  
Noureddine Takorabet

► **To cite this version:**

Paisak Poolphaka, Ehsan Jamshidpour, Thierry Lubin, Lotfi Baghli, Noureddine Takorabet. Influence of High-Frequency Operation on the Efficiency of a PMSM Drive with SiC-MOSFET Inverter. *Energies*, 2024, 17 (10), pp.2347. 10.3390/en17102347. hal-04573915

**HAL Id: hal-04573915**

<https://hal.univ-lorraine.fr/hal-04573915v1>

Submitted on 4 Sep 2024

**HAL** is a multi-disciplinary open access archive for the deposit and dissemination of scientific research documents, whether they are published or not. The documents may come from teaching and research institutions in France or abroad, or from public or private research centers.





L'archive ouverte pluridisciplinaire **HAL**, est destinée au dépôt et à la diffusion de documents scientifiques de niveau recherche, publiés ou non, émanant des établissements d'enseignement et de recherche français ou étrangers, des laboratoires publics ou privés.



Distributed under a Creative Commons Attribution 4.0 International License

## Article

# Influence of High-Frequency Operation on the Efficiency of a PMSM Drive with SiC-MOSFET Inverter

Paisak Poolphaka <sup>1,2</sup>, Ehsan Jamshidpour <sup>1</sup> , Thierry Lubin <sup>1,\*</sup> , Lotfi Baghli <sup>1</sup>  and Nouredine Takorabet <sup>1</sup> 

<sup>1</sup> Université de Lorraine-GREEN, F-54000 Nancy, France; paisak@eng.src.ku.ac.th (P.P.); ehsan.jamshidpour@univ-lorraine.fr (E.J.); lotfi.baghli@univ-lorraine.fr (L.B.); noureddine.takorabet@univ-lorraine.fr (N.T.)

<sup>2</sup> Faculty of Engineering, Sriracha Campus, Kasetsart University Chonburi 20230, Thailand

\* Correspondence: thierry.lubin@univ-lorraine.fr; Tel.: +33-3-727-450-95

**Abstract:** This paper investigates the effects of high-frequency switching and a high fundamental frequency on the parameters and efficiency of a high-speed permanent magnet synchronous machine (PMSM) drive. We discuss the design and modeling of the PMSM, taking into account these high-frequency effects. The impact of high frequencies is analyzed across three different inverters (IGBT, Fast IGBT, and SiC-MOSFET) and the motor, and we employ theoretical analysis, computer simulations, and experimental tests for validation. Our goal is to enhance our understanding of how these high-frequency factors affect the performance of the motor drive.

**Keywords:** PMSM drive; high-speed motor; SiC-MOSFET inverter



**Citation:** Poolphaka, P.; Jamshidpour, E.; Lubin, T.; Baghli, L.; Takorabet, N. Influence of High-Frequency Operation on the Efficiency of a PMSM Drive with SiC-MOSFET Inverter. *Energies* **2024**, *17*, 2347. <https://doi.org/10.3390/en17102347>

Academic Editors: Loránd Szabó and Marcin Wardach

Received: 29 March 2024

Revised: 25 April 2024

Accepted: 10 May 2024

Published: 13 May 2024



**Copyright:** © 2024 by the authors. Licensee MDPI, Basel, Switzerland. This article is an open access article distributed under the terms and conditions of the Creative Commons Attribution (CC BY) license (<https://creativecommons.org/licenses/by/4.0/>).

## 1. Introduction

In recent years, the automotive industry has undergone a significant transformation, and we are witnessing a notable shift towards electric propulsion systems aimed at curbing greenhouse gas (GHG) emissions and combating climate change. With transportation heavily relying on internal combustion engines (ICEs) in vehicles, which are responsible for approximately 14% of global GHG emissions [1], efforts are underway to address carbon emissions by transitioning towards alternative sustainable power sources. Electric vehicles (EVs) have emerged as a promising solution by offering a cleaner and more sustainable mode of transportation compared to traditional internal combustion engine vehicles.

Simultaneously, the aerospace sector is experiencing a paradigm shift towards more electrified technologies to minimize emissions, fuel consumption, and operational expenses. The aviation industry is a significant contributor to global greenhouse gas emissions and is responsible for 2.5% to 3.5% of total emissions, with 90% attributed to commercial aircraft operations [2]. Consequently, the aviation sector has initiated a technological transition towards electrification known as “More Electric Aircraft” (MEA). By substituting electrical energy for mechanical, pneumatic, and hydraulic power sources, this electrified approach has demonstrated potential fuel savings of up to 9% [3,4].

Hybrid and turboelectric propulsion architectures for aircraft have been studied to facilitate a transition towards more electric propulsion systems, potentially leading to the development of all-electric aircraft. This evolution mirrors the transition from hybrid electric vehicles (HEVs) to fully electric vehicles (EVs), with HEVs serving as pioneers in the shift from traditional fuel-based vehicles to EVs. However, the aerospace industry demands electrical systems with higher power levels, energy densities, and power densities compared to the automotive industry. Moreover, every component onboard an aircraft must operate with maximum reliability under diverse conditions [3].

Within the realm of EV and MEA technologies, permanent magnet synchronous motors (PMSMs) have garnered attention for their remarkable torque density, power density, and efficiency. High-speed PMSMs, renowned for their efficient operation at

elevated rotational speeds, have become integral components in modern EV powertrains and MEA applications. PMSMs' ability to deliver high power output at elevated speeds enhances EVs' acceleration and performance, thus improving the overall driving experience for consumers. However, addressing mechanical strength issues in the rotors of high-speed interior PM (IPM) motors during the initial design phase is crucial [5].

One significant challenge of high-speed motor drives involves raising the motor's fundamental frequency. While this enhances the motor's power density, it also poses limitations, such as increased iron losses [6,7]. The impact of frequency on iron losses and calculation methods are presented in [8–10]. Additionally, raising the fundamental frequency reduces the inverter's frequency modulation index, affecting the current waveform in the motor phases and leading to increased total harmonic distortion (THD), resulting in additional losses and torque ripples. Addressing these challenges involves increasing the inverter's switching frequency to improve current THD. However, there are limits to increasing the switching frequency depending on the power electronic devices used.

Furthermore, the compact design and lightweight construction of high-speed PMSMs contribute to the overall efficiency and range of electric vehicles by minimizing energy losses and maximizing power delivery [11–13]. Advancements in motor control algorithms and power electronics have further optimized the performance of high-speed PMSMs, facilitating their seamless integration into next-generation electric propulsion systems [14,15].

The effects of high switching frequencies on the performance of power electronics converters have been extensively studied in various papers across different applications. In [16,17], the nonlinearities in SiC-based three-phase inverters and IGBT-based inverters are studied and compared by considering factors such as dead time, switching delay time, switching frequency, and output parasitic capacitance. The authors of [18] investigated the impact of dead time on SiC-BJT and SiC-MOSFET on converter losses in a high-frequency resonant converter. Additionally, ref. [19] presents an analysis of parasitic elements, their categorization, and their effects on the operation of a high-frequency DC-DC buck converter for EV applications. Their results indicate that parasitic elements can affect the power loop, gate loop, and overall efficiency of the converter.

This paper aims to explore the design and modeling of a high-speed PM motor drive to identify the optimum frequency for maximum efficiency. To do this, two identical PMSM motors are mechanically coupled together. One motor operates as a motor, drawing power from a DC source via a three-phase inverter, while the other acts as a generator, supplying a resistive load to act as a mechanical load for the first motor. To investigate the effects of high frequencies, including both switching and fundamental frequencies, on the entire system—comprising the inverter and motor—we utilize three inverters, each constructed with different components (IGBT, Fast IGBT, and SiC-MOSFET).

In the subsequent section, we investigate the impact of frequency variation on the inverters, followed by an examination of machine design and the influence of the frequency on machine performance. Additionally, our study assesses the effects of high-frequency current on motor losses (both mechanical and electrical) through comprehensive modeling and experimentation. Subsequently, the designed motor undergoes testing using the inverters at various fundamental and switching frequencies to validate theoretical and simulation findings. Finally, we analyze the implications of frequency variation on the combined operation of the drive and motor.

The remainder of this paper is structured as follows: Section 2 presents the effect of frequency variation on the drive of a PMSM. Section 3 provides a detailed discussion of the design and modeling of the studied PMSM. Modeling PMSM losses across frequency variations is discussed in Section 4. Section 5 explores the influence of high frequencies on PMSM drives based on the simulation and experimental results. Finally, Section 6 summarizes the findings and offers concluding remarks.

## 2. Frequency Variation Effect on the Drive of a PMSM

The effects of varying switching and fundamental frequencies on the performance of a driver (inverter) can be classified into three categories:

- Voltage drop on the output voltage, affecting the speed control of the PMSM;
- Increase in total harmonic distortion for voltage and current, impacting the performance of the PMSM;
- Influence on the driver losses, subsequently affecting the efficiency of the entire system.

In this section, we investigate these effects.

### 2.1. Influence on the Output Voltage Drop

Various imperfections inherent in a 3Ph\_VSI, such as dead times between switching signals, switching times, voltage drops induced by power switches (IGBT, SiC, and diode), and the impact of parasitic capacitances contribute to the voltage drop observed at the output terminal of a VSI. Figure 1 depicts a leg of a VSI. This voltage drop, attributed to imperfections, is denoted as  $\Delta v_{an_{err}}$  and represents the disparity between the actual output voltage ( $v_{an}$ ) and the ideal output voltage ( $v_{an}^*$ ) anticipated from an optimized inverter:

$$\Delta v_{an_{err}} = \Delta v_1 + \Delta v_2 + \Delta v_3 + \Delta v_4 = v_{an} - v_{an}^* \quad (1)$$

- $\Delta v_1 = -V_{dc} \left( \frac{t_d}{T_s} \right)$ , where  $t_d$  and  $T_s$  represent the dead time and switching period, respectively. This voltage drop signifies the average voltage drop over one modulation period (PWM) attributed to dead times (the yellow parts in Figure 2).
- $\Delta v_2 = -V_{dc} \left( \frac{t_{on} - t_{off}}{T_s} \right) \text{sign}(i_a)$ , where  $t_{on}$  and  $t_{off}$  are the turn-on time and the turn-off time, respectively. This term denotes the average voltage drop resulting from component switching times (the red part is due to  $t_{off}$ , and the green part is due to the  $t_{on}$  in Figure 2).
- $\Delta v_3 = -(V_{SW} \cdot D + V_{FD} \cdot (1 - D)) \text{sign}(i_a)$ , where  $D$  is the duty cycle,  $V_{SW}$  and  $V_{FD}$  represent the voltage drop across a conducting switch (blue area in Figure 2) and the voltage drop across the conducting diode (violet area in Figure 2), respectively. This voltage signifies the average voltage drop arising from voltage drops across power switches.
- $\Delta v_4$  indicates the average voltage drop caused by the effects of parasitic capacitances.

Figure 2 illustrates the different voltage drops in the output voltage. Based on the results presented in [16,17], this voltage drop increases as the switching frequency increases. Therefore, at higher speeds for which the motor requires more voltage, this may pose a problem. For further details on these effects, please refer to [16,17], which provides a comprehensive explanation.

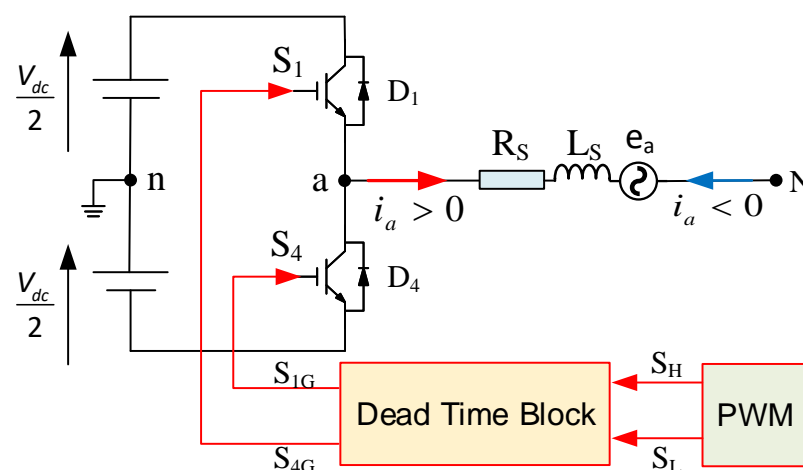
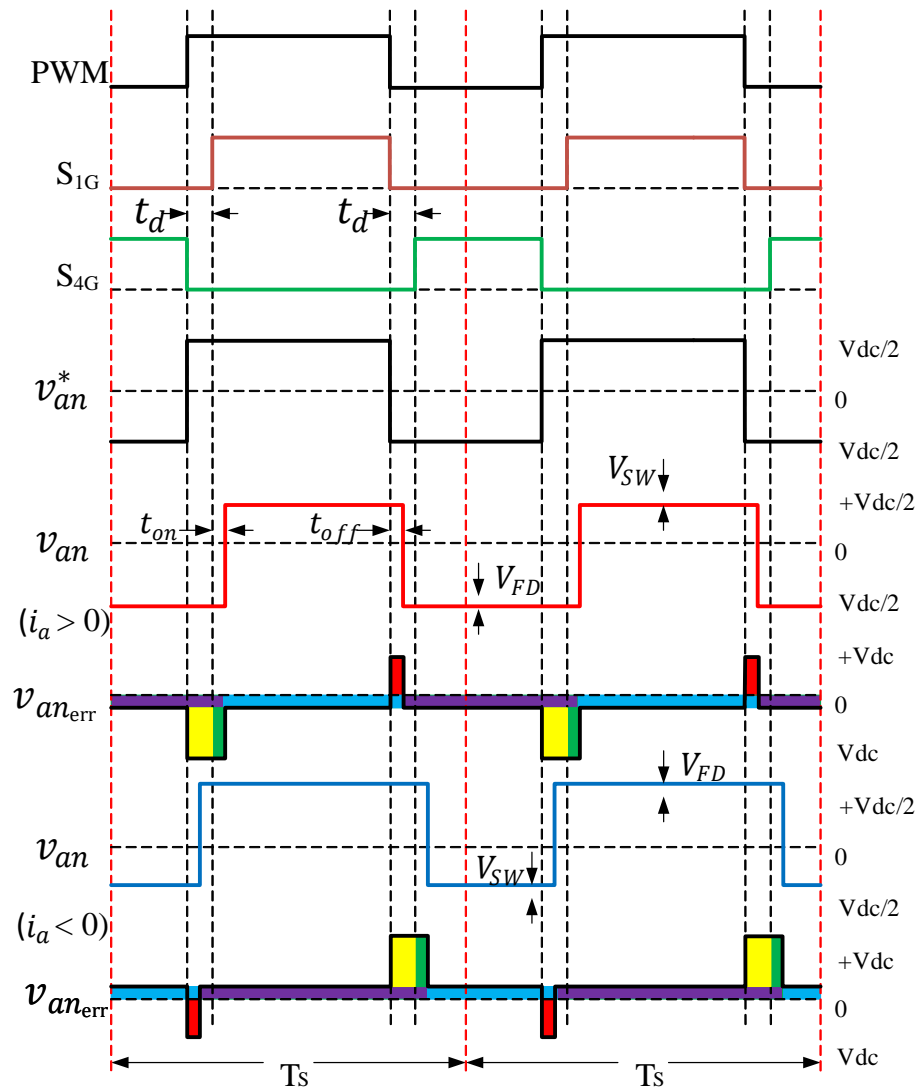


Figure 1. A-phase leg of three-phase inverter with the dead-time block.



**Figure 2.** Waveform of the output voltage taking into account voltage drops, dead time, switching times, and parasitic capacitors [17].

## 2.2. Influence on the Voltage and Current Total Harmonic Distortion

The authors of [17] also explored the impact of varying the PWM frequency and dead time on the total harmonic distortion (THD) within the voltage and current waveforms of inverters constructed using IGBT, Fast IGBT, and SiC-MOSFET.

As the PWM frequency increases while maintaining a constant dead time, the fundamental voltage decreases, leading to an escalation of THD. Comparing THD measurements among the three inverters under similar operational conditions in Figure 3, we consistently identify the SiC-MOSFET inverter as exhibiting the highest THD. However, the ability to decrease the dead time, a characteristic associated with SiC-MOSFET components, notably enhances THD performance. Notably, setting the dead time to  $0.5 \mu\text{s}$  maintains the THD at 95% across different PWM frequencies [17].

Furthermore, the investigation delves into the influence of dead time on low-frequency voltage harmonics (5th and 7th orders) and their subsequent impact on current waveforms. Experimental findings, as illustrated in Figure 4, unveil a linear correlation between dead time and the amplification of these harmonics [17].

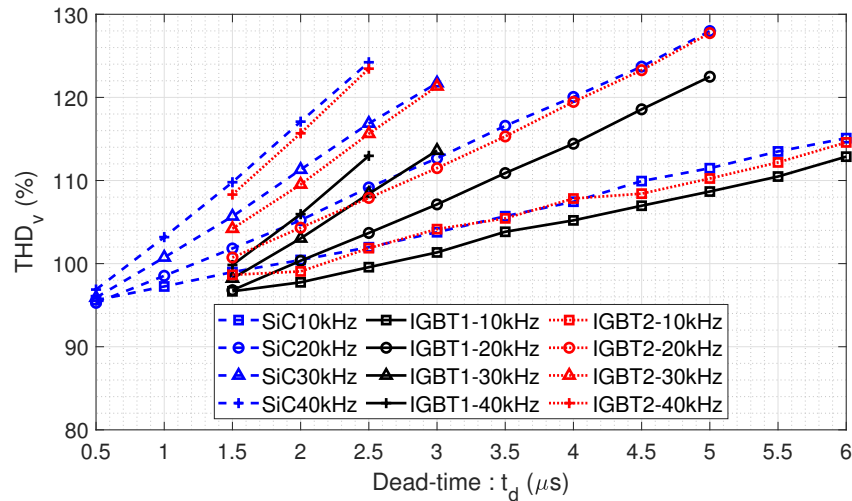


**Figure 3.** Comparison of the  $THD_v$  (total harmonic distortion of the voltage) for the SiC-MOSFET, IGBT, and Fast IGBT inverters varying with dead time and at different PWM frequencies [17].

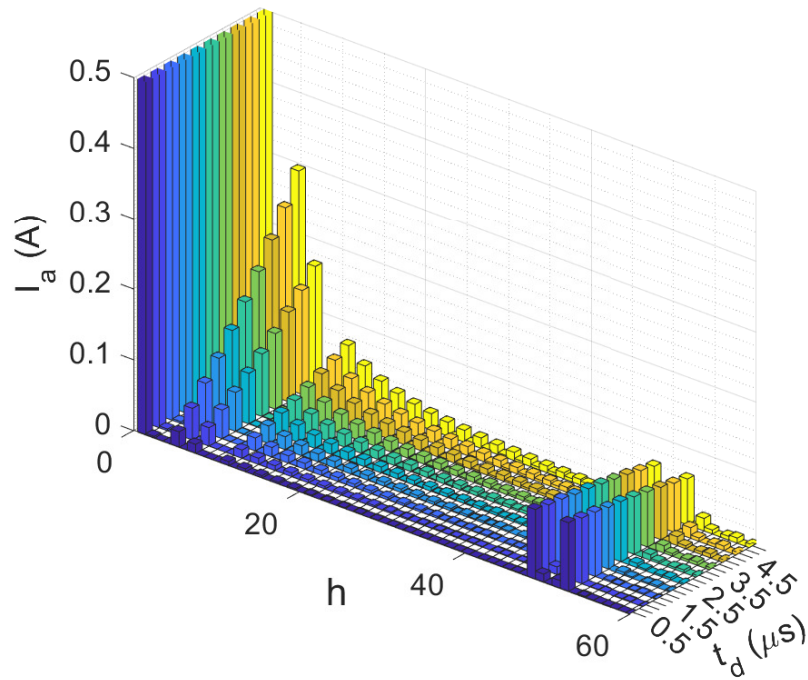


**Figure 4.** Experimental measurement of the current spectrum for various dead time ( $t_d$ ) values [17].

### 2.3. Influence on the Inverter Losses and Efficiency

In general, losses in power semiconductor switches are categorized into two groups: static losses and dynamic losses. Static losses comprise conduction losses (power losses during on-state) and off-state losses, while dynamic losses include turn-on and turn-off losses. However, off-state losses in the switch are typically much lower than the on-state losses due to minimal leakage current. For instance, referring to the datasheet of the Fast IGBT (SKM100GB125DN), with a collector current ( $I_c$ ) of 100 A, the dissipated energy in the on-state ( $E_{on}$ ) is approximately 25 mW, while for the off-state ( $E_{off}$ ), it is 5 mW. The most significant losses to be calculated in an IGBT and a SiC-MOSFET transistor are the conduction losses and switching losses.

#### 2.3.1. Conduction Losses of IGBT and SiC-MOSFET

During conduction, an IGBT comprises two components in series: a collector–emitter on-state resistance ( $r_{CE}$ ) and a DC voltage source ( $V_{CE0}$ ) representing the collector–emitter

voltage at zero current. Hence, the collector–emitter voltage ( $v_{CE}$ ) during on-state is given by:

$$v_{CE} = r_{CE} \cdot i_C + V_{CE0} \quad (2)$$

Consequently, the instantaneous conduction losses of the IGBT are:

$$p_{\text{cond}}^{\text{IGBT}}(t) = r_{CE} \cdot i_C^2(t) + V_{CE0} \cdot i_C(t) \quad (3)$$

The average conduction losses ( $P_{\text{cond}}^{\text{IGBT}}$ ) are obtained by integrating these instantaneous losses over the modulation period ( $T_s$ ), resulting in:

$$P_{\text{cond}}^{\text{IGBT}} = r_{CE} \cdot I_{C_{rms}}^2 + V_{CE0} \cdot I_{C_{avr}} \quad (4)$$

Here,  $I_{C_{rms}}$  and  $I_{C_{avr}}$  represent the RMS and average current, respectively, through the IGBT during conduction. To calculate the conduction losses of a SiC-MOSFET, the same method can be used, yielding the following equation.

$$P_{\text{cond}}^{\text{SiC-MOSFET}} = R_{DS_{on}} \cdot I_{D_{rms}}^2 \quad (5)$$

### 2.3.2. Switching Losses of IGBT and SiC-MOSFET

The average switching losses in the IGBT can be calculated using the following equation, where  $f_s$  represents the PWM frequency:

$$P_{sw}^{\text{IGBT}} = f_s \cdot (E_{on}^{\text{IGBT}} + E_{off}^{\text{IGBT}}) \quad (6)$$

The losses dissipated during switching in an IGBT,  $E_{on}^{\text{IGBT}}$  and  $E_{off}^{\text{IGBT}}$ , are provided in the manufacturer's datasheets in the form of data graphs. However, most of these data are obtained under test conditions (voltage, current, and reference junction temperature) that typically differ from the inverter's operating conditions. Therefore, by utilizing the reference values provided in the datasheets, the energy losses during switching can be estimated using the following empirical relationships.

$$E_{on}^{\text{IGBT}} = E_{on\_ref} \left( \frac{i_C}{I_{ref}} \right)^{K_i} \left( \frac{V_{DC}}{V_{ref}} \right)^{K_v} [1 + TC_{sw}(T_j - T_{jref})] \quad (7)$$

$$E_{off}^{\text{IGBT}} = E_{off\_ref} \left( \frac{i_C}{I_{ref}} \right)^{K_i} \left( \frac{V_{DC}}{V_{ref}} \right)^{K_v} [1 + TC_{sw}(T_j - T_{jref})] \quad (8)$$

where:

- $V_{ref}, I_{ref}, T_{jref}$ : reference values indicated by the manufacturer;
- $E_{on\_ref}, E_{off\_ref}$ : energy dissipated in the IGBT for the reference values;
- $K_i$ : exponent of current dependency ( $\approx 1$ );
- $K_v$ : exponent of voltage dependency ( $\approx 1.3$ – $1.4$ );
- $TC_{sw}$ : temperature coefficient ( $\approx 0.003$ ).

Expressions (7) and (8) are generally obtained for IGBTs placed within a chopper circuit where the reference current  $I_{ref}$  is continuous in steady-state (excluding ripple). To use these relationships for an inverter where the current in the load is alternating in steady-state, we consider an "equivalent" current  $i_C$  equal to the average value of the load current over half a period of the fundamental frequency, assuming a sinusoidal load current with RMS value  $I_{C_{rms}}$ , given by:

$$i_C = \frac{1}{\pi\sqrt{2}} I_{C_{rms}} \quad (9)$$

We then obtain:

$$E_{on}^{IGBT} = E_{on\_ref} \left( \frac{\sqrt{2}I_{C_{rms}}}{\pi I_{ref}} \right)^{K_i} \left( \frac{V_{DC}}{V_{ref}} \right)^{K_v} \left[ 1 + TC_{sw}(T_j - T_{jref}) \right] \quad (10)$$

$$E_{off}^{IGBT} = E_{off\_ref} \left( \frac{\sqrt{2}I_{C_{rms}}}{\pi I_{ref}} \right)^{K_i} \left( \frac{V_{DC}}{V_{ref}} \right)^{K_v} \left[ 1 + TC_{sw}(T_j - T_{jref}) \right] \quad (11)$$

To calculate the losses of a SiC-MOSFET, the same method can be used, which gives the following equations:

$$E_{on}^{SiC-MOSFET} = E_{on\_ref} \left( \frac{\sqrt{2}I_{D_{rms}}}{\pi I_{ref}} \right)^{K_i} \left( \frac{V_{DC}}{V_{ref}} \right)^{K_v} \left[ 1 + TC_{sw}(T_j - T_{jref}) \right] \quad (12)$$

$$E_{off}^{SiC-MOSFET} = E_{off\_ref} \left( \frac{\sqrt{2}I_{D_{rms}}}{\pi I_{ref}} \right)^{K_i} \left( \frac{V_{DC}}{V_{ref}} \right)^{K_v} \left[ 1 + TC_{sw}(T_j - T_{jref}) \right] \quad (13)$$

And finally, the SiC-MOSFET switching losses can be calculated using this equation:

$$P_{sw}^{SiC-MOSFET} = f_s \cdot (E_{on}^{SiC-MOSFET} + E_{off}^{SiC-MOSFET}) \quad (14)$$

### 2.3.3. Diode Losses

The energy losses associated with diode switching primarily occur during its reverse recovery when transitioning to the blocking state. Generally, energy losses during diode turn-on are much lower and can be disregarded. Therefore, the diode switching energy loss is also referred to as diode reverse recovery energy loss ( $E_{rr}^D$ ). Just like with IGBTs and SiC-MOSFETs, datasheets for diodes provide values for the energy dissipated in the diode during blocking,  $E_{rr\_ref}^D$ , for defined test conditions specified by  $I_{ref}$ ,  $V_{ref}$ , and  $T_{jref}$ . The method used to determine  $E_{rr}^D$  is the same as that followed for IGBTs and SiC-MOSFETs:

$$E_{rr}^D = E_{rr\_ref} \left( \frac{\sqrt{2}I_{F_{rms}}}{\pi I_{ref}} \right)^{K_i} \left( \frac{V_{DC}}{V_{ref}} \right)^{K_v} \left[ 1 + TC_{sw}(T_j - T_{jref}) \right] \quad (15)$$

thus:

$$P_{sw}^{diode} = f_s \cdot E_{rr}^D \quad (16)$$

with:

- $V_{ref}$ ,  $I_{ref}$ ,  $T_{j\_ref}$ : reference values indicated by the manufacturer;
- $E_{rr\_ref}^D$ : energy dissipated in the diode for the reference values;
- $K_i$ : exponent indicating current dependence ( $\approx 0.5-0.6$ );
- $K_v$ : exponent indicating voltage dependence ( $\approx 0.6$ );
- $TC_{sw}$ : temperature coefficient ( $\approx 0.006$ ).

In each period of switching, during the dead time, a diode conducts to maintain the continuity of the current in the load. Therefore, during the dead time, the conduction losses can be determined as follows:

$$P_{cond}^{dead} = 2 \cdot t_d \cdot f_s \left( \frac{(r_F \cdot I_p^2)}{4} + \frac{V_{F0} \cdot I_p}{\pi} \right) \quad (17)$$

where  $I_p$  is the maximum value of the current in one phase.



### 2.3.4. Total Losses and Inverter Efficiency

To calculate the inverter losses, it is essential to determine the RMS and average currents through both the switch and the diode based on the inverter's operational parameters. Assuming a balanced three-phase load connected to the inverter output with sufficient inductance to filter the high-frequency harmonics of the PWM, the load current can be assumed sinusoidal:

$$i_a(t) = I_p \sin(\omega_1 t - \varphi) \quad (18)$$

Here,  $I_p$  represents the maximum output current of the inverter,  $\omega_1$  is the fundamental frequency of the current, and  $\varphi$  denotes the phase difference between the current and the fundamental component of the voltage.

It is important to note that the conduction time of a component within one PWM period varies and relies on the duty cycle, which is given by:

$$D(t) = \frac{1}{2}[1 + m_a \sin(\omega_1 t)] \quad (19)$$

Here,  $m_a$  stands for the amplitude modulation index. The expressions for the switch current ( $i_{sw}$ ) and diode current ( $i_F$ ) in the inverter can be described using Equations (20):

$$\begin{cases} i_{sw} = D(t) \cdot i_a(t) \\ i_F = (1 - D(t)) \cdot i_a(t) \end{cases} \quad (20)$$

The average current through a switch (IGBT or SiC-MOSFET) and a diode are calculated over half of the fundamental current period:

$$\begin{cases} I_{sw_{ave}} = I_p \left( \frac{1}{2\pi} + \frac{m_a \cos(\varphi)}{8} \right) \\ I_{F_{ave}} = I_p \left( \frac{1}{2\pi} - \frac{m_a \cos(\varphi)}{8} \right) \end{cases} \quad (21)$$

The RMS current value through a switch and diode are obtained by:

$$\begin{cases} I_{sw_{rms}} = I_p \sqrt{\frac{1}{8} + \frac{m_a \cos(\varphi)}{3\pi}} \\ I_{F_{rms}} = I_p \sqrt{\frac{1}{8} - \frac{m_a \cos(\varphi)}{3\pi}} \end{cases} \quad (22)$$

Starting from the total conduction losses  $P_{cond}^{total}$  and total switching losses  $P_{sw}^{total}$  calculated within a switch and a diode, the overall losses of the inverter can be obtained as:

$$P_{loss}^{inv} = (P_{cond}^{total} + P_{sw}^{total}) \times 6 \quad (23)$$

where:

$$P_{cond}^{total} = P_{cond}^{switch} + P_{cond}^{diode} + P_{cond}^{dead} \quad (24)$$

$$P_{sw}^{total} = P_{sw}^{switch} + P_{sw}^{diode} \quad (25)$$

If we consider the RMS value of the output voltage fundamental based on the voltage drop due to imperfections ( $\Delta V$ ), the current in the purely sinusoidal load, and the power factor of the load, the inverter output power ( $P_{out}^{inv}$ ) is given by:

$$P_{out}^{inv} = 3 \left( \frac{m_a V_{dc}}{2\sqrt{2}} - \frac{4\Delta V}{\pi\sqrt{2}} \right) \frac{I_p}{\sqrt{2}} \cos(\varphi) = \frac{3}{2} \left( \frac{m_a V_{dc}}{2} - \frac{4\Delta V}{\pi} \right) I_p \cos(\varphi) \quad (26)$$

where  $\Delta V$  is [17]:

$$\Delta V_{a_{N1}} = V_{a_{ref}} - \frac{-2V_{a1} \cos \varphi \pm \sqrt{(2V_{a1} \cos \varphi)^2 + 4(V_{a_{ref}}^2 - V_{a1}^2)}}{2} \quad (27)$$

The efficiency calculation is straightforward and is obtained by power balance:

$$\eta = \frac{P_{out}^{inv}}{P_{out}^{inv} + P_{loss}^{inv}} \quad (28)$$

### 3. Studied PMSM Motor Design and Modeling

Exploring high-speed aspects in powertrains entails a multifaceted approach considering mechanical stress, vibration, thermal effects, and electrical/magnetic characteristics. However, this paper delves specifically into the ramifications of escalating the fundamental frequency of electrical quantities without venturing into extremely high-speed realms, thus circumventing intricate mechanical concerns for now. Our aim is to achieve frequencies surpassing 1 kHz while upholding mechanical speeds within the range of a few thousand revolutions per minute. To realize this objective, we opt to amplify the number of pole pairs in the machine and target fundamental frequencies of 2 kHz and speeds of 6000 rpm, with a power target of approximately 6 kW for the laboratory-scale bench.

Expanding the number of pole pairs confers several advantages, including downsizing the dimensions of the back iron (yoke) in both the stator and rotor armatures, thereby shedding weight from the machine and enhancing torque density. Furthermore, leveraging fractional-slot windings, such as the 48 coils–40 poles configuration considered here, bolsters torque density by curtailing end-windings. Table 1 provides the main specifications of the machine.

**Table 1.** Main specifications of the PMSM.

Parameter	Value
Rated power	6 kW
Maximal Power	10 kW
Rated speed	6000 rpm
Number of poles	40
Number of slots	48
Rated frequency	2000 Hz
Switching frequency	20–100 kHz
DC Voltage	540 V
Mass	2.5 kg

Analytical pre-design, based on standard rules, furnishes the initial machine parameters. Distinctive design features such as small teeth between coils to enhance heat transfer between the coils and ambient, segmented and resin-embedded magnets, and a specialized shaft assembly design are employed. Finite element analysis aids with pinpointing critical parameters, ensuring stable performance even at high switching frequencies and speeds.

To address AC losses, the coils are crafted with multiple strands in series, reducing the wire diameter relative to skin depth. Careful slot arrangement regulates inter-turn voltage, curbing EMI challenges. These strategies bolster efficiency and streamline dynamic control, which are crucial for high-speed applications. Figure 5 provides separate views of the stator and rotor prior to assembly.

With a high number of rotor poles and the resulting hollow structure, the machine exhibits a low moment of inertia, yielding a pronounced mechanical dynamic response. Precision in shaft assembly poses a key challenge and necessitates specialized mechanical design, as illustrated in the following figure, and emphasizes the need for meticulous centering of the two half-shafts.

To counter AC losses from the skin effect in the stator winding, the coils employ multiple series strands with smaller cross-sections. This design ensures that the wire diameter remains significantly smaller than the skin depth. Furthermore, orderly wire arrangement within slots regulates the inter-turn voltage, reducing high  $dv/dt$  and mitigating capaci-

tive behavior of the stator winding, thus alleviating EMI challenges associated with high switching frequencies. Figure 6 illustrates the stator winding.

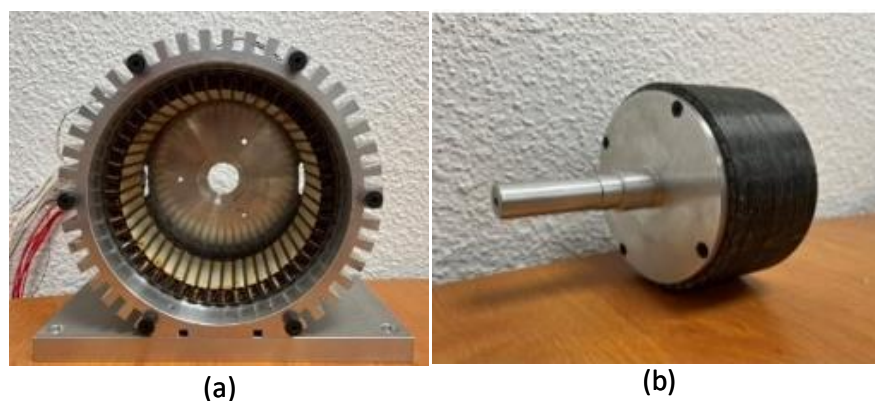


**Figure 5.** (a) Stator of PMSM. (b) Rotor of PMSM.

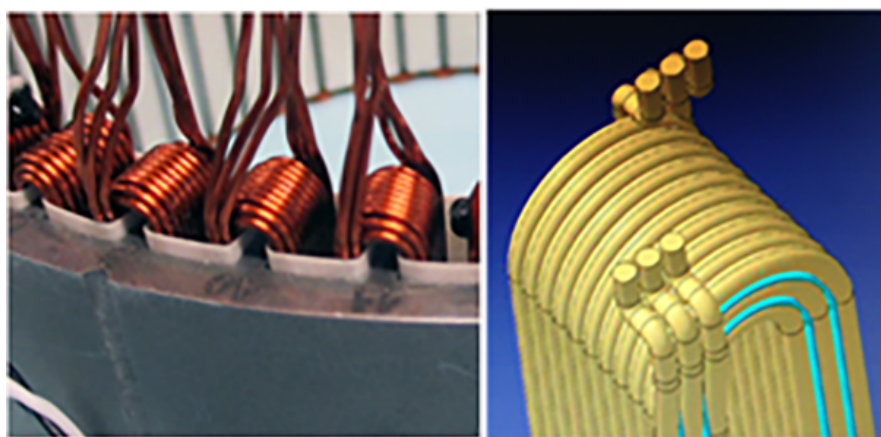


**Figure 6.** Wire arrangement in the slots (3 wires in hand per turn).

In the motor design process, the consistent dimensions obtained from the analytical pre-sizing process serve as the foundation. Initially, a simplified 2D analytical model with an equivalent current-sheet is employed to represent the stator armature winding currents. This analytical model is then integrated with the MATLAB 2022b Optimization Toolbox to derive the primary dimensions of the machine, including the pole-pair number, the outer radius of the rotor, the magnet thickness, the air-gap length, and the axial length of the machine, in accordance with the specifications. Subsequently, finite element method (FEM) simulations using FEMM 4.2 software are utilized to account for slotting effects and magnetic saturation of the iron parts, while the adjustment of other dimensions of the machine (such as stator teeth, stator, and rotor back-iron thicknesses) is carried out to optimize performance. As an example, Figure 7 shows the flux density distribution at no-load obtained with FEMM software.

Figure 8 depicts the shape of the back-electromotive forces (EMFs) under no-load conditions at a speed of 5000 rpm along with the waveform of the electromagnetic torque. The torque waveform corresponds to when the currents are in phase with the EMFs, which is achieved through vector control in maximum torque per ampere (MTPA) mode ( $I_d = 0$ ,  $I_q = 13$  A), representing 75% of the rated power.

Finite element analysis (FEA) facilitates the identification of crucial machine parameters: particularly, the inductances  $L_d$  and  $L_q$ . These inductances are observed to be nearly identical and demonstrate minimal sensitivity to variations in stator currents ( $L_d \approx 0.26$  mH and  $L_q \approx 0.27$  mH), as shown in Figure 9. This slight difference is mainly due to a higher saturation level in the d-axis due to the auxiliary flux with the rotor magnet. The design

objective for this machine prioritized maintaining constant parameters relative to stator currents with the aim of simplifying control implementation and reducing the CPU time required for regulation loops. This emphasis on swift control execution proves essential, especially when dealing with very high switching frequencies (up to 100 kHz) at the highest speeds.

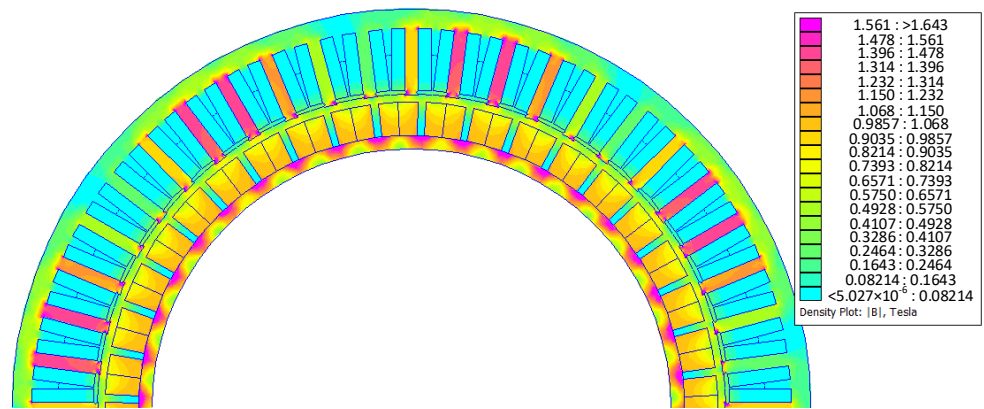


Figure 7. Flux density distribution at no-load obtained with FEMM software.

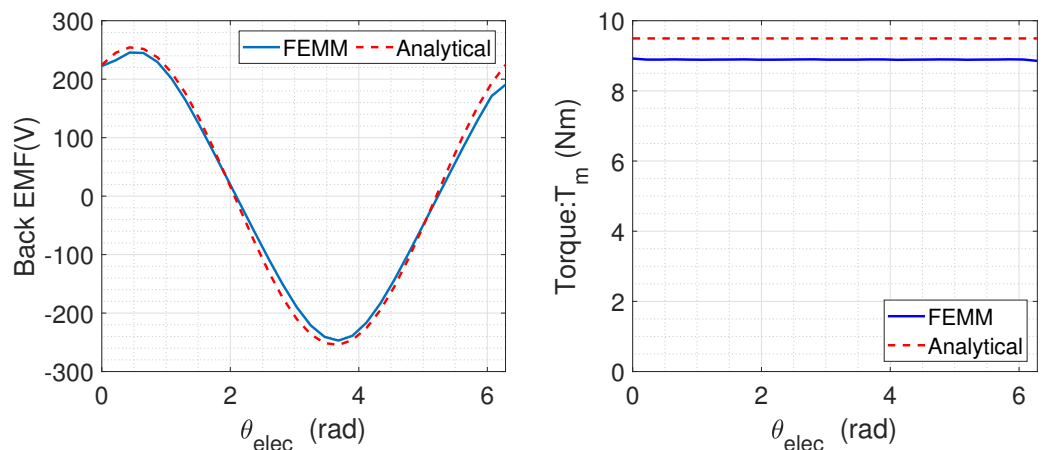


Figure 8. Back-EMF and torque waveforms at 5000 rpm,  $I_q = 13$  A.

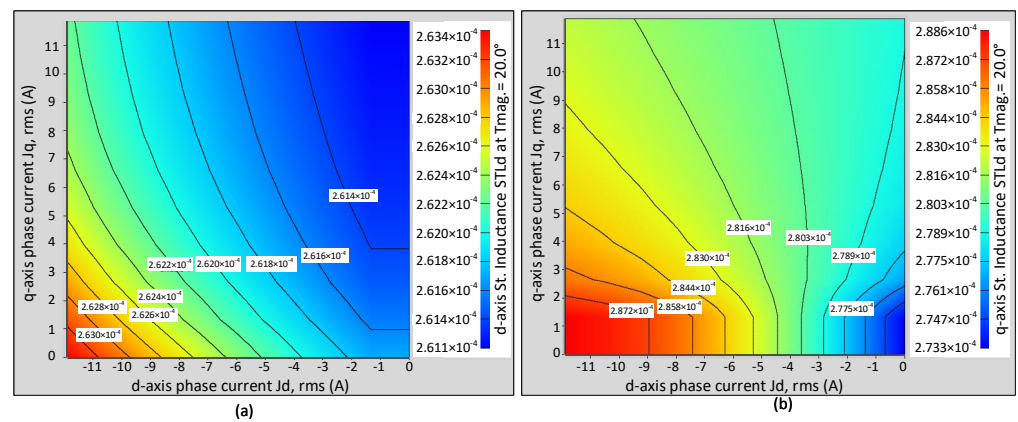


Figure 9. Mapping of: (a)  $L_d(i_d, i_q)$  and (b)  $L_q(i_d, i_q)$ .

#### 4. Modeling PMSM Losses across Frequency Variations

##### 4.1. Copper Losses with Impact of Skin Effect

The phenomenon of skin effect induces a non-uniform distribution of current density within conductors, diminishing the effective cross-sectional area of the conductor and consequently increasing electrical resistance to current flow. In this context, selecting an appropriate conductor diameter is crucial to minimize losses attributed to the skin effect. The skin depth, denoted by  $\delta$ , is defined as follows:

$$\delta = \frac{1}{\sqrt{\pi f \mu_0 \sigma_c}} \quad (29)$$

Here:

- $\sigma_c$  represents the electrical conductivity of copper;
- $\mu_0$  stands for the magnetic permeability of vacuum ( $4\pi \times 10^{-7}$  Wb/Am).

The impact of the skin effect is evaluated by the ratio of the conductor resistances in AC and DC ( $R_{AC}/R_{DC}$ ). This ratio is termed the resistance factor or Kelvin coefficient [20] and is commonly denoted as ( $K_R$ ).

Figure 10 vividly illustrates how the resistance factor ( $K_R$ ) escalates with the frequency of the current flowing through the winding conductors. Consequently, the skin effect amplifies the phase resistance, leading to heightened resistive losses. Figure 10 is plotted based on the parameters of the analyzed machine.

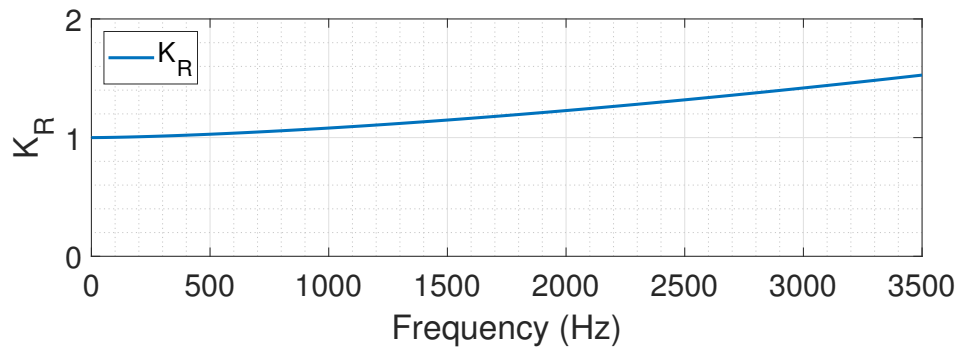


Figure 10. Resistance factor as a function of frequency.

The correlation between resistances concerning frequency is established through the influence of these coefficients on the DC resistances:

$$R_s(f) = K_R(f) \times R_s(dc) \quad (30)$$

Here,  $R_s(f)$  represents the AC resistances, while  $R_s(dc)$  denotes the DC resistance. That is why the stator windings are designed with three wires in hand, as illustrated in Figure 6.

##### 4.2. Iron Losses

Iron losses in electrical machines primarily arise from the magnetic fluxes generated by the magnets and are typically classified as eddy current losses and hysteresis losses. Particularly in high-frequency machines, these iron losses can exceed resistive losses. Effective strategies to mitigate these losses often involve adjusting the sheet thickness or optimizing material properties.

The core material of the machine consists of an iron–cobalt alloy with a saturation induction of approximately 2.2 T. Specifically, the stator employs VACOFLUX 48, while the rotor utilizes VACODUR 49, which, though slightly less efficient, still boasts excellent mechanical and magnetic characteristics.

The iron loss characteristics are depicted in Figure 11. At a frequency of 400 Hz, VACOFLUX 48 exhibits losses of approximately 30 W/kg. This value significantly rises to around 150 W/kg at a frequency of 1000 Hz, marking a fivefold increase. To estimate the iron losses, Steinmetz’s equation [21] can be utilized, as shown in Equation (31):

$$P_{IR} = k_H \cdot f \cdot B_M^2 + k_F \cdot f^2 \cdot B_M^2 \tag{31}$$

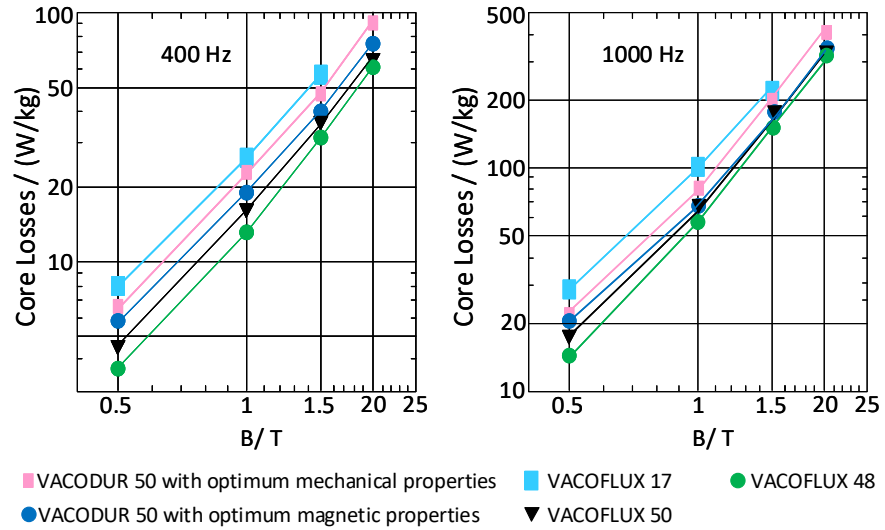


Figure 11. Iron loss characteristics of various iron alloys.

The coefficients  $k_H$  and  $k_F$  are derived from the material characteristics datasheet at different frequencies.

Figure 12 demonstrates nonlinear increases in losses that have been extrapolated using the coefficients provided by the manufacturer within the Steinmetz model.

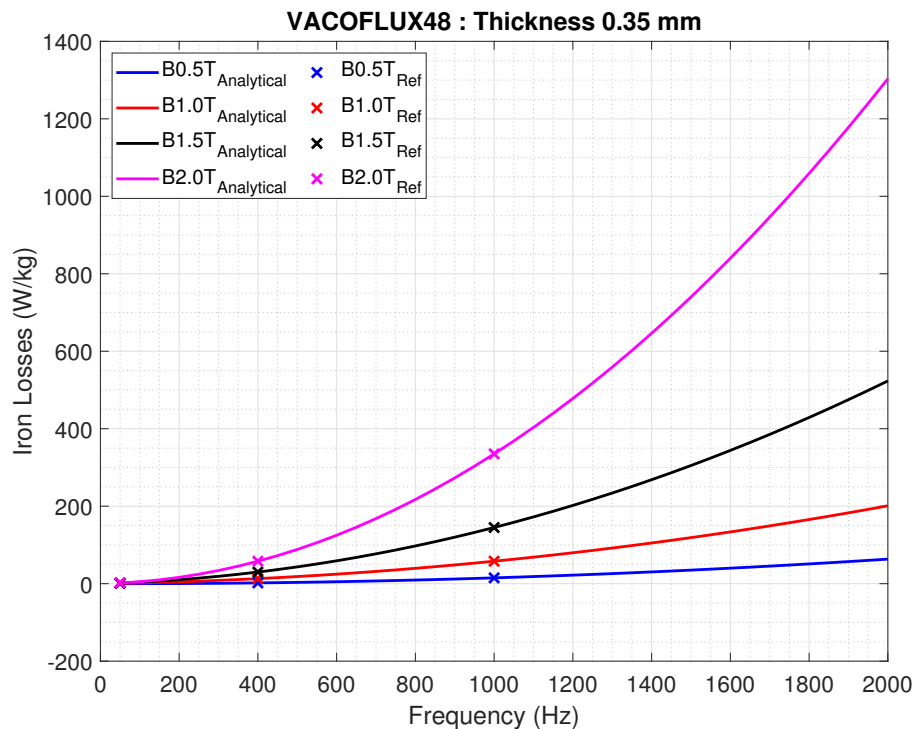


Figure 12. Frequency-specific iron losses for studied machine.

#### 4.3. Mechanical Losses

The rotation of the rotor results in mechanical losses; these are primarily attributed to friction. These losses are classified into aerodynamic losses within the air gap ( $P_a$ ), rolling losses in bearings ( $P_b$ ), and friction losses ( $P_{fs}$ ).

$$P_{mec} = P_a + P_b + P_{fs} \quad (32)$$

Aerodynamic losses in the air gap are caused by air friction and are expressed as:

$$P_a = k_r \pi \rho_{air} C_f L (R_a - e)^4 \Omega^3 \quad (33)$$

where  $C_f$  is the coefficient of friction given by:

$$C_f = \begin{cases} \frac{5 \left( \frac{e}{R_a - e} \right)^{0.3}}{R_{rey}} & \text{if } R_{rey} < 64 \\ \frac{\left( \frac{e}{R_a - e} \right)^{0.3}}{R_{rey}^{0.6}} & \text{if } 64 < R_{rey} < 500 \\ 0.515 \frac{\left( \frac{e}{R_a - e} \right)^{0.3}}{R_{rey}^{0.5}} & \text{if } 500 < R_{rey} < 10000 \end{cases} \quad (34)$$

Frictional losses in bearings ( $P_b$ ) are given by:

$$P_b = \frac{\Omega M}{1000} = \frac{\Omega(M_0 + M_1)}{1000} \quad (35)$$

where  $M_0$  and  $M_1$  are two types of friction moments:

$$M_0 = \mu_{b0} \times 10^{-7} (v N_r)^{2/3} d_m \text{ (N}\cdot\text{mm)} \quad (36)$$

$$M_1 = \mu_{b1} F d_m \text{ (N}\cdot\text{mm)} \quad (37)$$

Friction losses ( $P_{fs}$ ) are expressed as:

$$P_{fs} = \Gamma_{fs} \Omega \quad (38)$$

Table 2 provides the essential parameters required for calculating mechanical losses, while Figure 13 illustrates the correlation between rotor speed and mechanical losses. The red curve, which represents total mechanical losses, exhibits a notable escalation with increasing rotor speed, highlighting their importance in high-speed machinery. It is recommended to conduct experimental evaluations for precise determination of mechanical losses.

**Table 2.** Parameters for the calculation of mechanical losses.

Parameters	Value
Bearing-dependent coefficient: $\mu_{b0}$	13.8
Lubricant viscosity: $v$	10 (mm <sup>2</sup> )/s
Average bearing diameter: $d_m$	31 mm
Coefficient of friction: $\mu_{b1}$	0.0015
Load placed on bearings: $F$	16.088 N
Rotation speed: $N_r$	6000 rpm

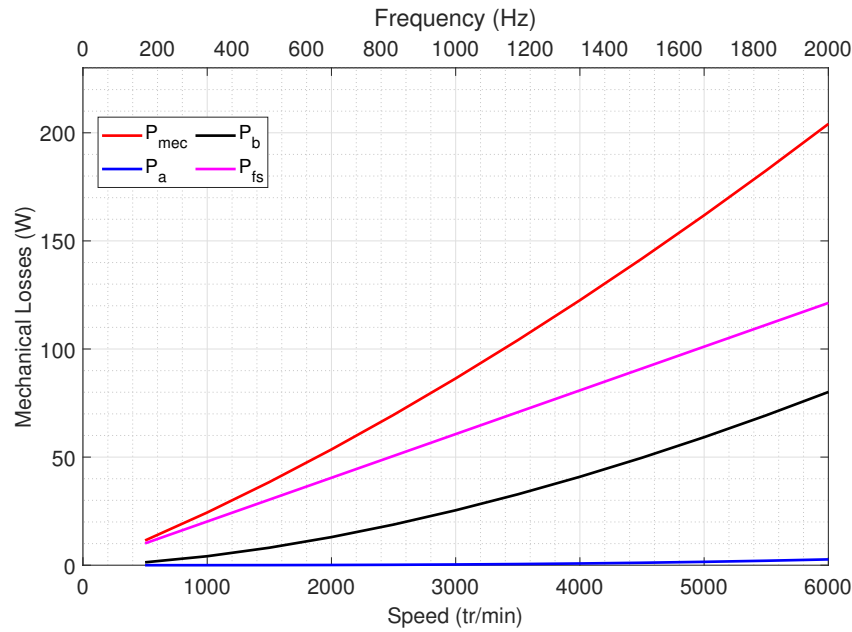


Figure 13. Variation of mechanical losses with rotor speed.

4.4. Total Losses

By combining the copper, iron, and mechanical losses, we derive the total losses of the machine as a function of frequency:

$$P_{Losses} = P_{Copper} + P_{IR} + P_{mec} \tag{39}$$

where  $P_{Copper}$ ,  $P_{IR}$ , and  $P_{mec}$ , respectively, are given by Equations (30)–(32). Integrating the results depicted in Figure 9 for copper losses (with  $R_{dc} = 0.26 \Omega$ ), in Figure 12 for iron losses (with  $B_{mean} \approx 1 \text{ T}$  in accordance with Figure 7), and in Figure 13 for mechanical losses, we obtain the total losses under the full load condition ( $I_q = 16 \text{ A}$ ) as a function of speed, as depicted in Figure 14. It is observed that mechanical and iron losses become predominant for speeds greater than 4000 rpm ( $f = 1333 \text{ Hz}$ ), while Joule losses remain constant across frequencies, hovering around 70 W, due to the stator winding wire diameter remaining significantly smaller than the skin depth.

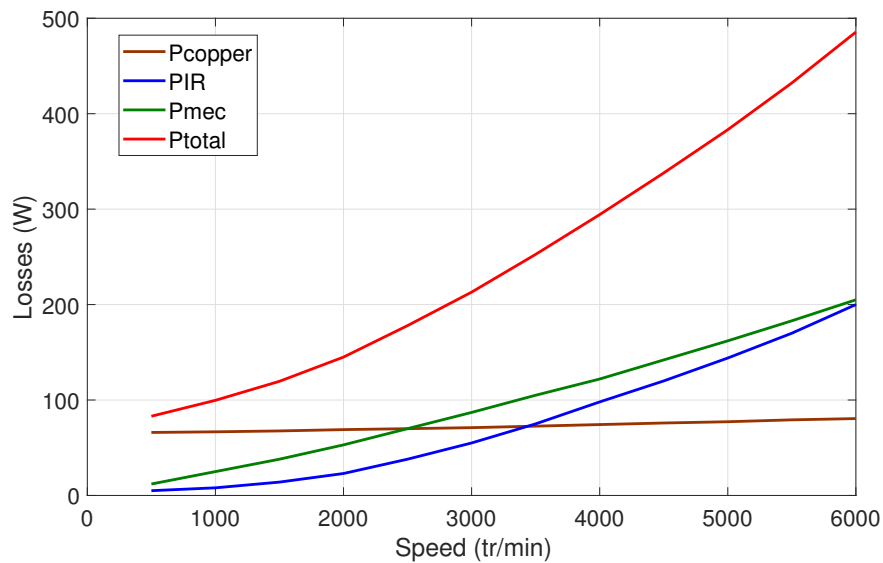


Figure 14. Copper, iron, mechanical, and total losses.



## 5. Simulation and Experimental Results

In this section, we delve into the modeling and experimental implementation of a high-frequency permanent magnet synchronous motor (PMSM) powered by an inverter. The objective is to investigate the impact of frequency (both switching and fundamental) on the inverter's performance. To achieve this, three distinct inverters are designed, built, and tested; each is constructed with different components: IGBT, Fast IGBT, and SiC-MOSFET, with detailed parameters outlined in Table 3. The drivers that are used for the IGBTs and the SiC-MOSFET are SKHI23/12R and CGD15FB45P1, respectively.

**Table 3.** Parameters of the three different inverters.

Parameter	IGBT SEMiX251GD126HD	Fast IGBT SKM100GB125DN	SiC-MOSFET CCS050M12CM
$V_{CE}$ or $V_{DS}$ (V)	1200	1200	1200
$I_C$ or $I_D$ (A) at 25 °C	242	100	87
$I_F$ (A) at 25 °C	207	95	102
$r_{CE}$ or $r_{DS(on)}$ (m $\Omega$ )	7	22.5	25
$r_F$ (m $\Omega$ )	5	11.1	20
$V_{CE0}$ (V)	0.9	2.3	0
$V_{F0}$ (V)	1.1	1	1.5
$E_{onref}$ (mJ)	37	11	1.1
$E_{offref}$ (mJ)	22	4	0.6
$E_{rrref}$ (mJ)	12	4	-
$t_{on}$ (ns)	295	75	51
$t_{off}$ (ns)	625	600	69
$R_G$ ( $\Omega$ )	10	10	20

The system is powered by a Lambda-TDK 600  $V_{DC}$ , 6000 W DC source and is managed through a dSPACE MicroLabBox DS1202. Typically, the MicroLabBox is programmed using the ControlDesk 2022-B software from dSPACE, which is constrained to generate higher switching frequencies. To circumvent this limitation, dSPACE offers the Real-Time Library (RTLib): a C runtime library functioning as a sublayer of RTI. This allows users to directly code in C language and utilize RTLib functions to access the DSP board hardware, granting full control over program execution on the DSP board. In this paper, we employ this approach to implement essential components of field-oriented control to incorporate high-frequency PWM and sampling rates ranging from 100 to 200 kHz to efficiently drive motors and power electronics. For further details, refer to [22].

Regarding the motor setup, we utilize two identical permanent magnet machines. One operates in motor mode, while the other acts as a generator connected to a three-phase resistive load, thereby serving as a load for the system under test. Positioned between the two permanent magnet machines is a torque meter, designated as  $T_L$ , which accurately measures the torque exerted on the shaft. Additionally, the electrical power consumption of both the machine and inverter is meticulously monitored using a power analyzer: specifically, the Tektronix PA4000 model (Tektronix, Beaverton, OR, USA).

The experimental setup used to validate the drive of the PMSM at high frequencies is illustrated in Figure 15.

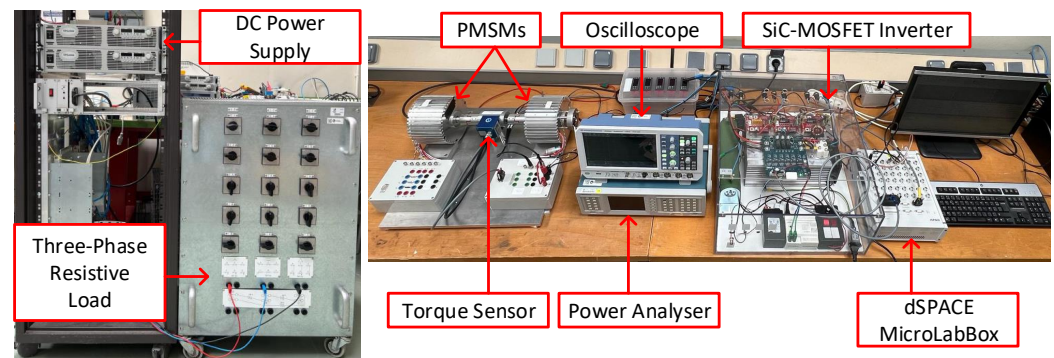


Figure 15. Experimental setup.

### 5.1. Inverter Losses and Efficiency Measurement

In this section, the results from the measurements of the losses and efficiency of each inverter are compared with those obtained from the analytical model shown in Equation (42), with the increase in switching frequency taken into account. The tests were conducted according to the diagram shown in Figure 16. The characteristics and parameters of the IGBTs, such as their resistances and dissipated energy, depend on temperature. For example, the resistance of the IGBT,  $r_{CE}$ , increases from  $4.7 \Omega$  to  $7.3 \Omega$  as the temperature ( $T_j$ ) rises from  $25^\circ\text{C}$  to  $150^\circ\text{C}$ . Therefore, to improve the accuracy of the analytical model, the temperature at the power switch ( $T_j$ ) is measured using a thermal camera (FLIR ONE<sup>®</sup> Pro LT (Täby, Sweden)) to determine the switching losses, as indicated in Equation (15). An example of the measured temperature for each inverter is illustrated in Figure 17.

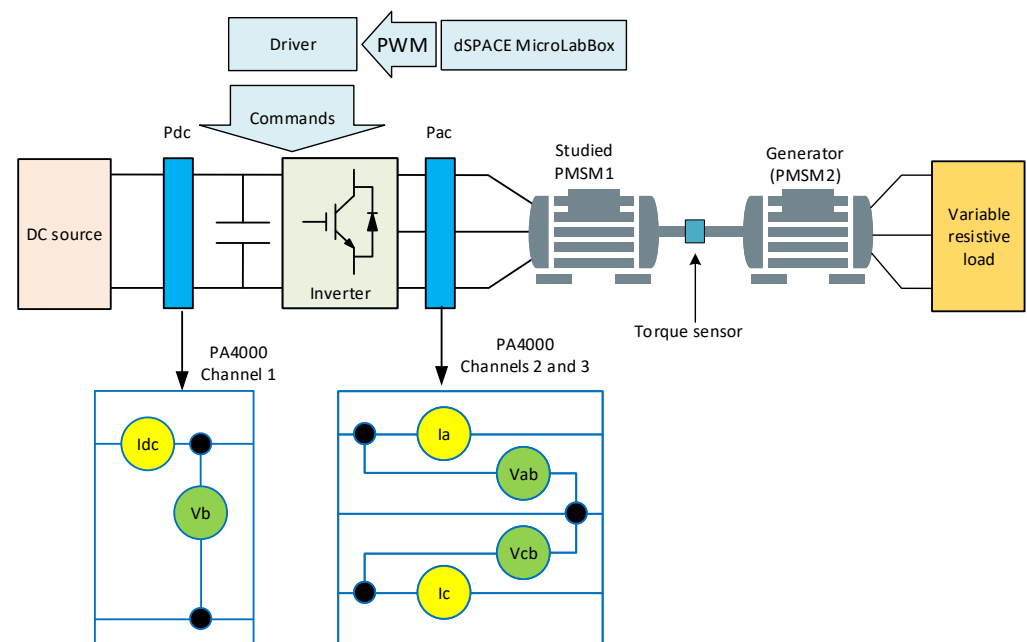


Figure 16. Diagram of the setup for efficiency measurement.

Figures 18–20 show a comparison of the efficiencies calculated by the analytical model and the measurements for the three inverters. It is observed that the losses are proportional to the power and that the efficiency of the inverter improves as the output power increases. For the IGBT inverter, a notable impact of the increase in PWM frequency on efficiency is observed, with efficiency dropping from 95.8% at full load and 10 kHz to less than 85% at 40 kHz for the same load.

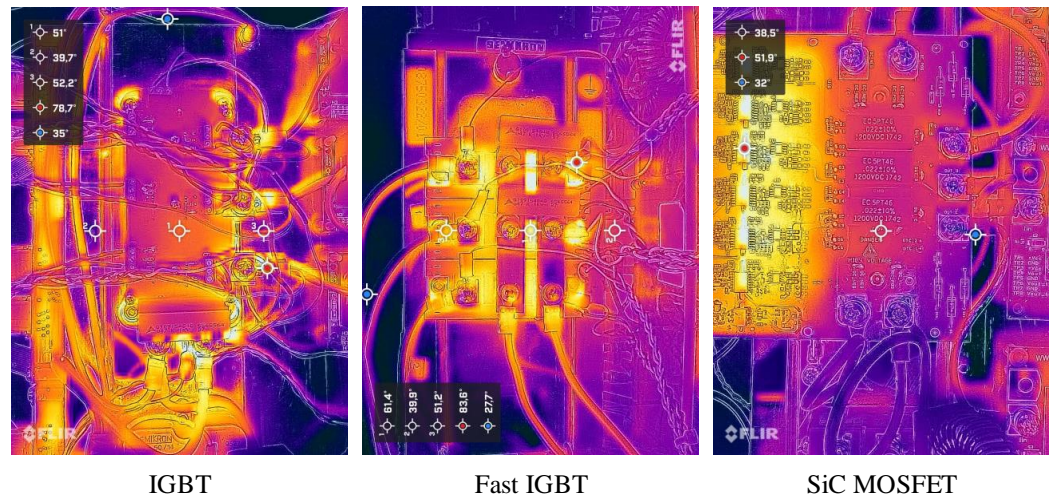


Figure 17. Measurement of the temperature of each inverter.

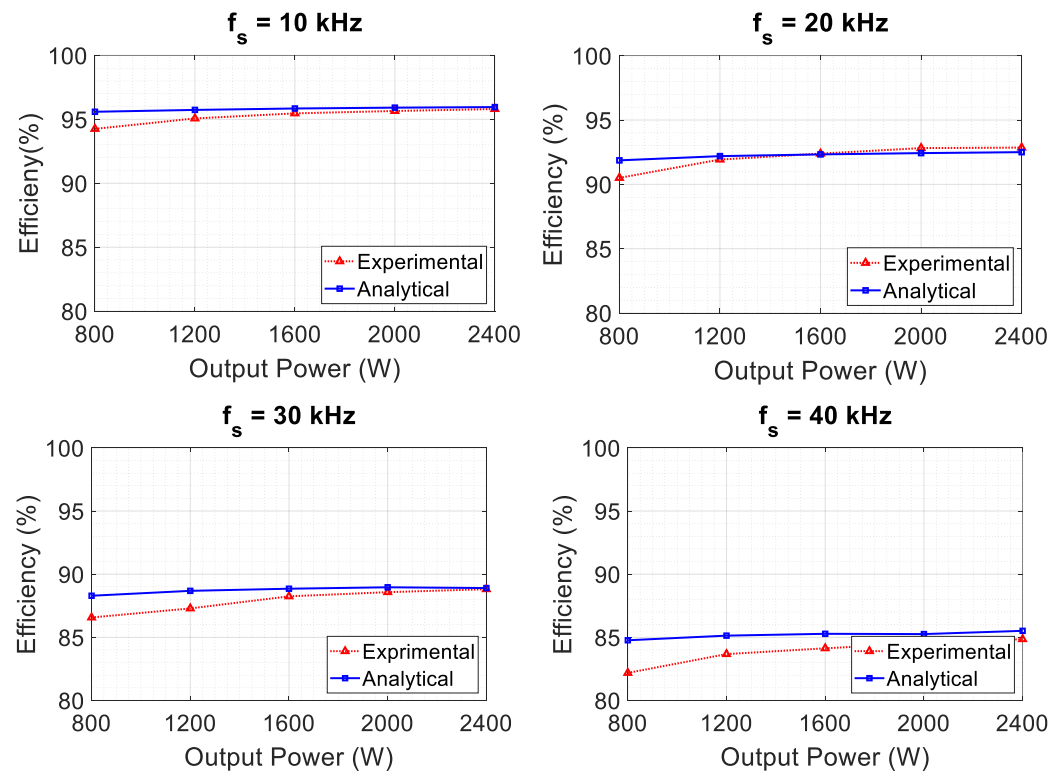


Figure 18. Efficiency of the IGBT inverter as a function of the output power for various values of the PWM frequency.

In Figure 19, it is evident that the model is less accurate at 40 kHz. Overall, and logically, given the superior performance of the components, the efficiency of the Fast IGBT inverter remains higher than that of the IGBT inverter.

Figure 20 illustrates the efficiency of the SiC-MOSFET inverter. Here, we observe that the efficiency obtained by the analytical model closely matches the measurements compared to the cases of the IGBT and Fast IGBT inverters. It is noteworthy that measurements become more challenging when losses are significantly lower. However, measurement errors are minimized thanks to the proper utilization of the PA4000 equipment (Beaverton, OR, USA).

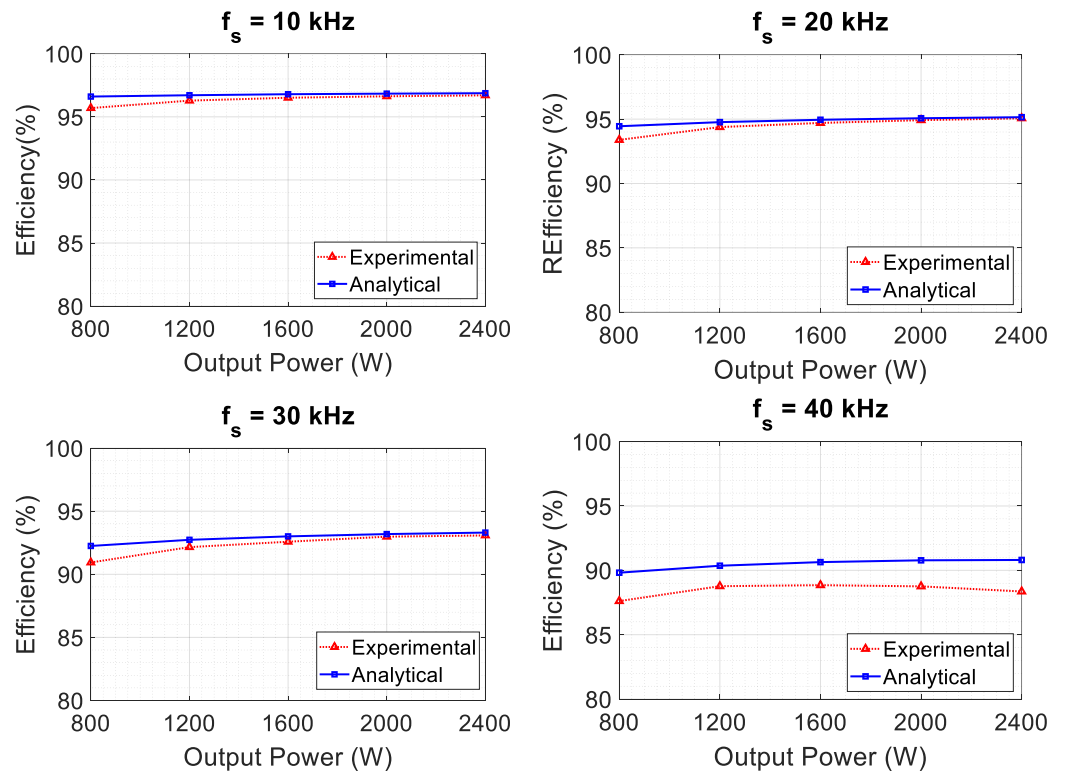


Figure 19. Efficiency of the Fast IGBT inverter as a function of the output power for various values of the PWM frequency.

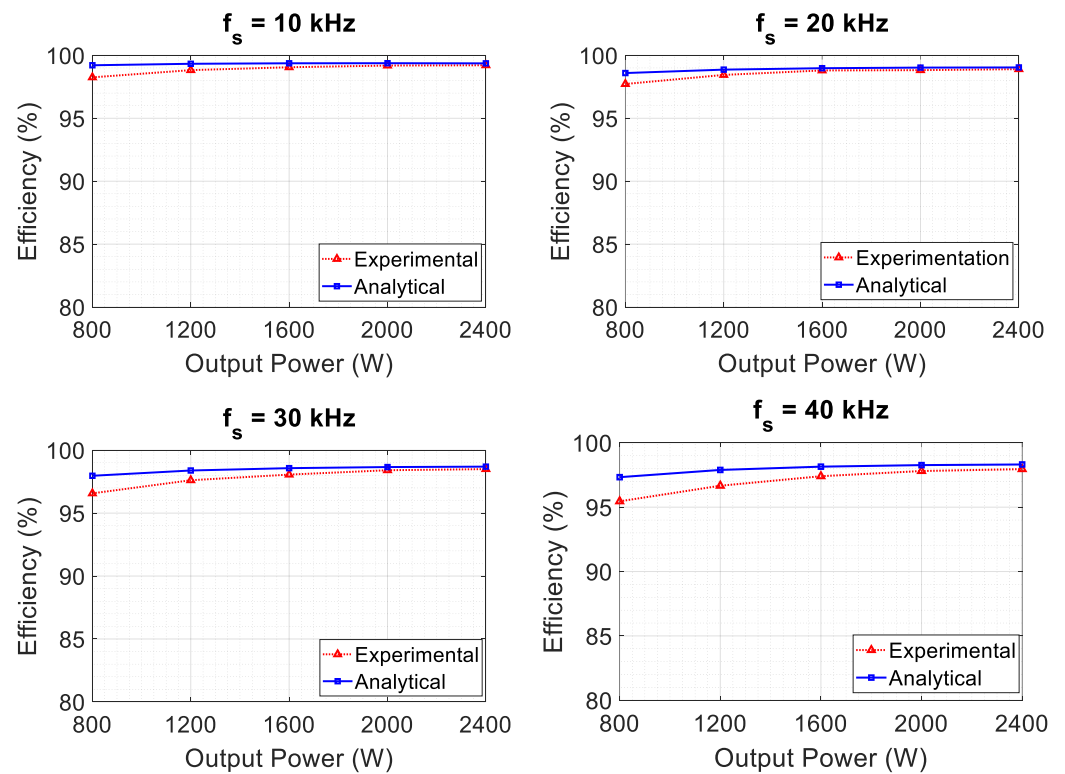


Figure 20. Efficiency of the SiC-MOSFET inverter as a function of the output power for various values of the PWM frequency.

### 5.2. Effect of Increasing Speed (Fundamental Frequency) on Current Distortion

For this series of experimental tests, the PMSM is controlled by field-oriented control (FOC), where the current and speed are regulated by PI controllers. An increase in rotor speed results in ripple in the dq-axis currents ( $i_{dq}$ ) and in the motor phase current. Here, we provide an example for three speeds: 1000, 2500, and 5000 rpm. In addition to speed, we analyze the effect of PWM frequency on current distortion (harmonic distortion and ripple) by selecting three values: 20, 40, and 100 kHz. The simulation results are presented in Figures 21–23.

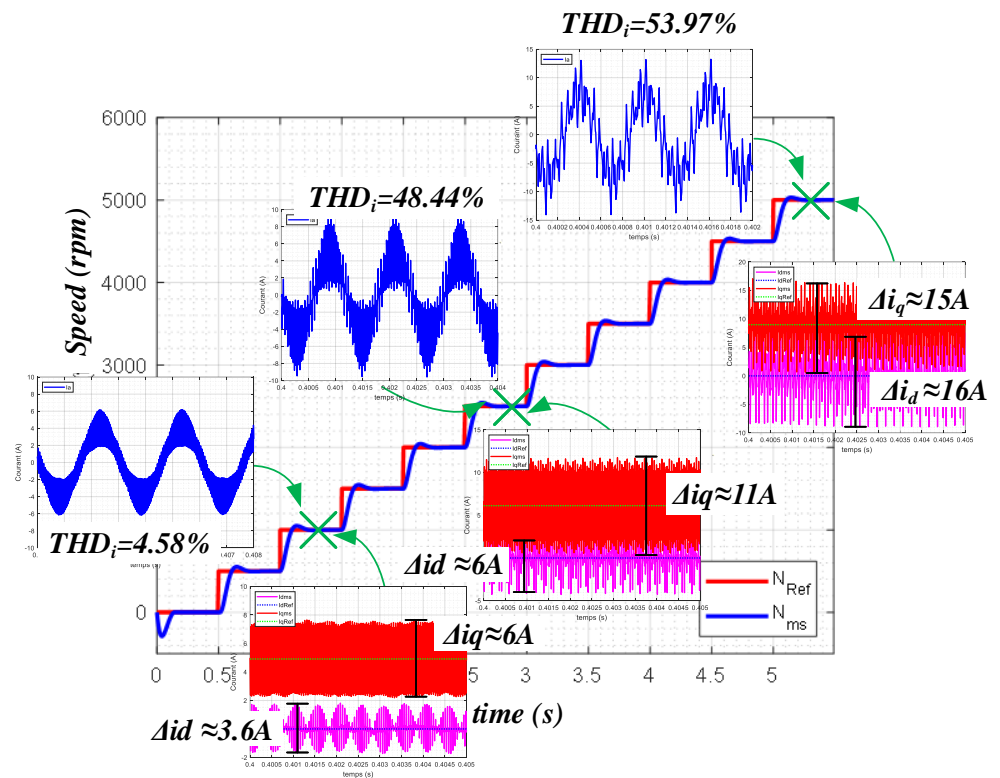


Figure 21. Current THD for  $f_s = 20$  kHz.

As depicted in Figure 21 for a switching frequency of 20 kHz, an increase in rotor speed corresponds to an increase in the electrical frequency of the motor phase current. The higher the electrical frequency, the lower the value of  $m_f$  ( $m_f = f_s / f_1$ ), leading to an increase in the harmonic distortion rate of the currents ( $THD_i$ ). This result is clearly observed at a motor speed of 5000 rpm ( $f_1 = 1667$  Hz,  $m_f = 12$ ,  $THD_i = 53.97\%$ ). The dq-axis currents ( $i_{dq}$ ) at 5000 rpm exhibit very high ripple rates ( $\Delta i_q = 15$  A and  $\Delta i_d = 16$  A). As mentioned in the previous section, increasing the switching frequency allows for a higher modulation index  $m_f$  to reduce  $THD_i$ .

The simulation results for a switching frequency of 40 kHz are presented in Figure 22. The  $THD_i$  and current ripple in the dq-axis ( $i_{dq}$ ) at a switching frequency of 40 kHz are lower than those obtained at a switching frequency of 20 kHz. At this switching frequency, some IGBT devices may still operate, but at significantly lower efficiencies. For this reason, SiC-MOSFET devices are used instead of IGBTs in high-frequency switching applications.

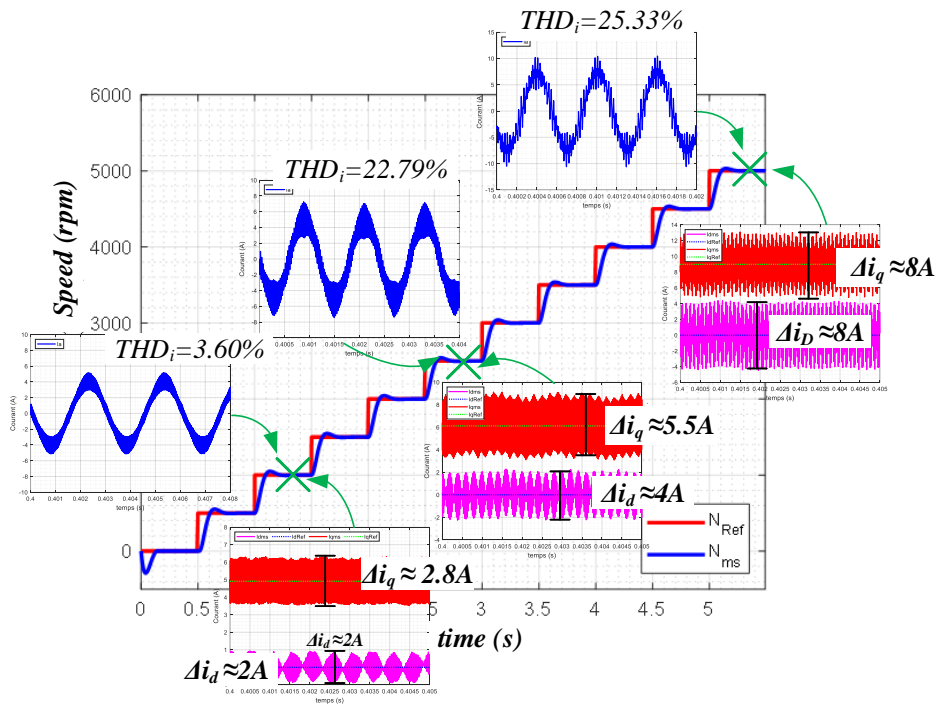


Figure 22. Current THD for  $f_s = 40$  kHz.

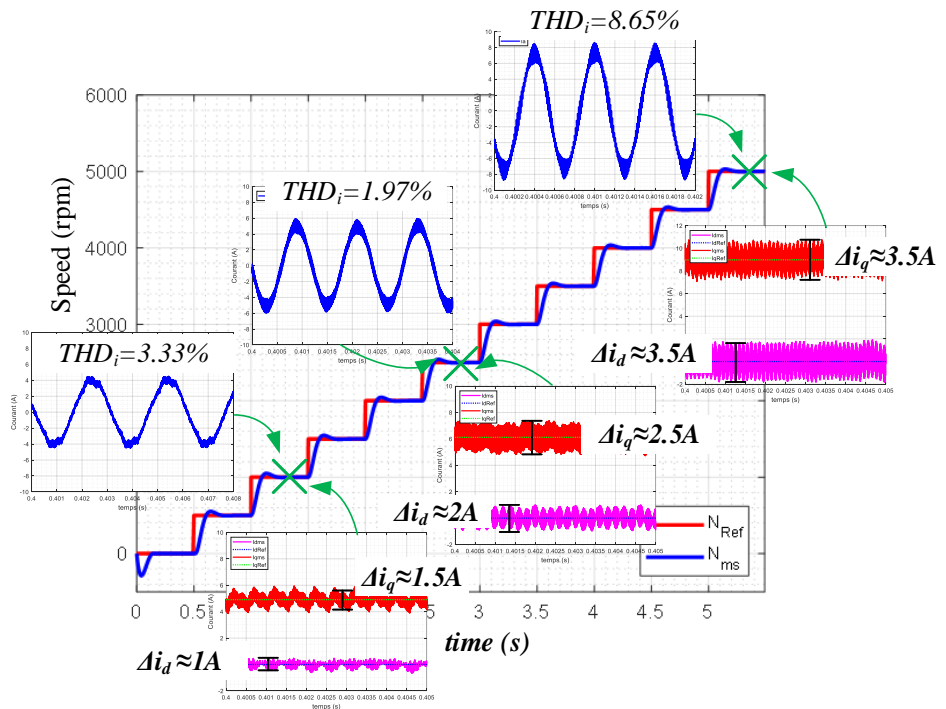


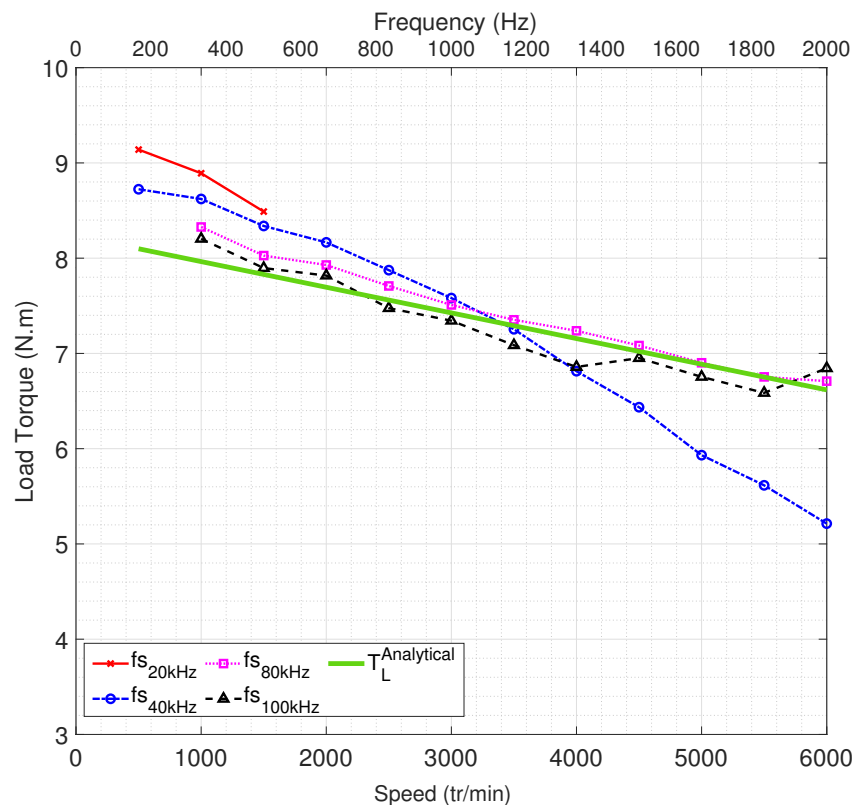
Figure 23. Current THD for  $f_s = 100$  kHz.

Figure 23 shows that at a switching frequency of 100 kHz, both  $THD_i$  and current ripple in the dq-axis ( $I_{dq}$ ) are significantly reduced. A comparison of the motor phase current  $THD_i$  at different switching frequencies and variable speeds is shown in Figure 24. In this test, the motor operates at its rated current ( $i_q = 16$  A), with speeds ranging from

500 RPM to 6000 RPM. Load torque ( $T_L$ ) is determined as the difference between the electromagnetic torque ( $T_m$ ) and the friction torque ( $T_f$ ):

$$T_L = T_m - T_f = k_t I_q - (f_0 + f_1 \Omega + f_2 \Omega^2) \quad (40)$$

Experimental and simulated load torques with  $I_q = 16$  A are shown in Figure 24. The load torque decreases linearly with increasing motor speed. Experiments at switching frequencies of 20 kHz, 40 kHz, 80 kHz, and 100 kHz reveal the influence of frequency on electromechanical conversion.



**Figure 24.** Load torque versus speed with  $I_q = 16$  A.

At low speeds, low-frequency switching yields high shaft torque. The torque sharply decreases at 40 kHz beyond 4000 RPM, but it remains consistent at 80 kHz and 100 kHz due to improved  $THD_i$ . The maximum error, 21.3%, occurs at 6000 RPM for 40 kHz. Limitation to 20 kHz results in rapid torque reduction at 2000 RPM due to the ripple in the  $I_q$  current, which could exceed the rated current of the PMSM.

### 5.3. PMSM Losses and Efficiency Measurement

Figure 25 compares the experimentally measured mechanical power to the analytical values. As expected, an increase in speed leads to a rise in mechanical power. Experimental results generally align with simulation except at a 40 kHz PWM frequency, where power starts decreasing above 4000 RPM due to reduced torque (Figure 24). At 20 kHz PWM, tests are capped at 1500 RPM, corresponding to a fundamental frequency of 750 Hz.

Mechanical and iron losses are evaluated by subtracting mechanical output power (torque and speed sensors) from input power (PA4000 power analyzer), adjusted for statoric resistive losses:

$$P_{mec} + P_{IR} = P_{in} - 3 \times R_s(f) \times I_{eff}^2 \quad (41)$$

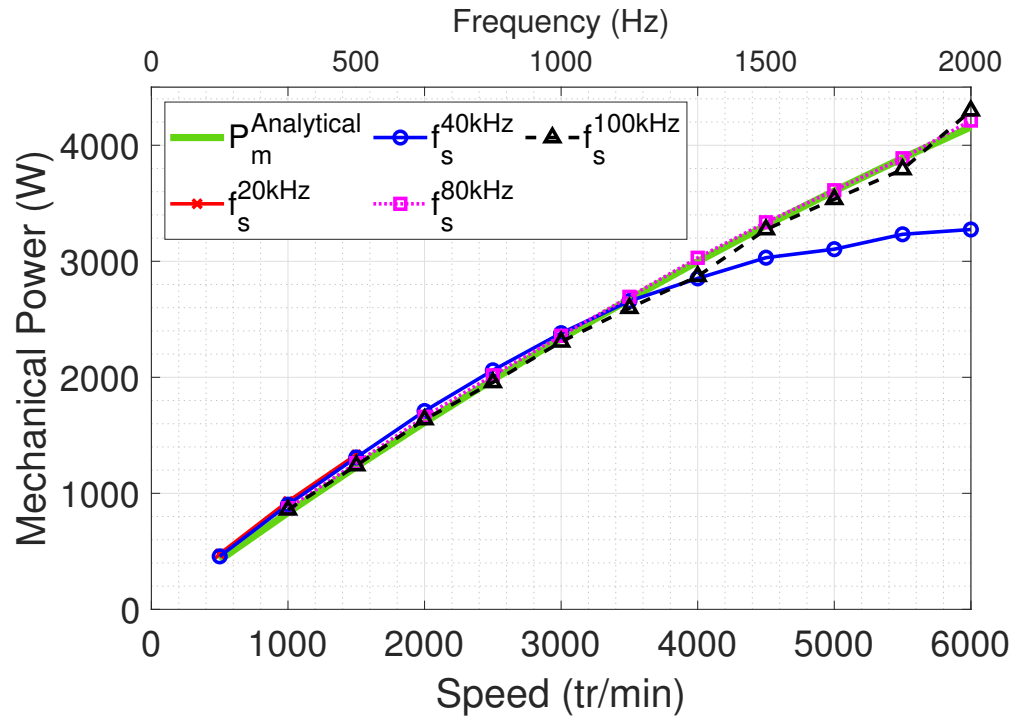


Figure 25. Mechanical power of the variable-speed PMSM.

The graph in Figure 26 compares the model’s predictions (shown in green) for motor losses, including both iron and mechanical losses, with actual test data obtained at different PWM frequencies:  $f_s = 40$  kHz (blue circle),  $f_s = 80$  kHz (purple square), and  $f_s = 100$  kHz (black triangle). The tests only provide the total losses, so iron and mechanical losses cannot be separated. As observed in Figure 26, when the PWM frequency is increased, iron losses decrease due to the reduction in current ripple. The lowest losses occur at  $f_s = 100$  kHz because the current waveforms become almost smooth and without ripples.

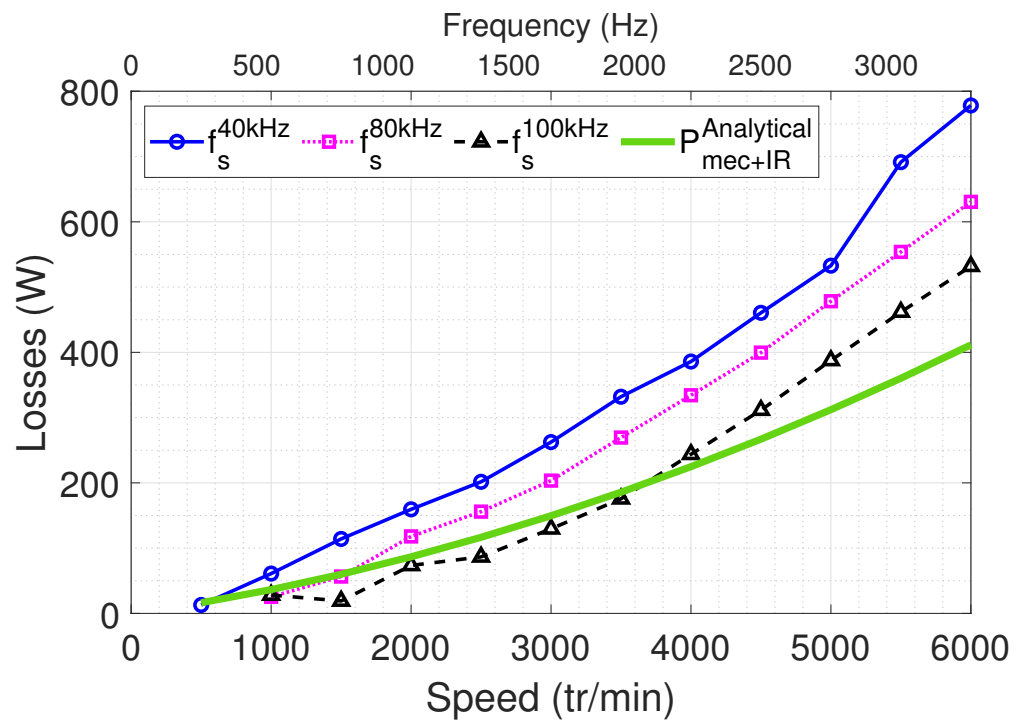


Figure 26. Iron losses + mechanical losses of the variable-speed PMSM.



The main causes of core losses are the magnetic field from the permanent magnets along with the effect of the stator currents. When the switching frequency is raised, the quality of the current improves by reducing unwanted components, which, in turn, reduces core losses. While losses in the magnets also decrease, they are not directly measured in this study. Instead, they are combined with core losses in the tests, which might explain why higher overall losses are observed in the experimental results shown in Figure 26.

Moreover, losses in the stator winding, which depend on the current and resistance that increase with frequency, need to be considered when calculating efficiency. Motor efficiency can be determined using Equation (42).

$$\eta = \frac{P_m}{P_m + P_{\text{joule}} + P_{\text{IR}} + P_{\text{mec}}} \times 100 \quad (42)$$

The results of these calculations and their comparison with experimental data are shown in Figure 27. At a switching frequency of 100 kHz, mechanical power is higher and losses are lower compared to other frequencies, which is consistent with previous findings. Consequently, the efficiency at 100 kHz is higher, and it gradually decreases with lower switching frequencies. Motor efficiency remains above 87% across the speed range: reaching over 90% between 1000 and 4000 rpm (see Figure 27).

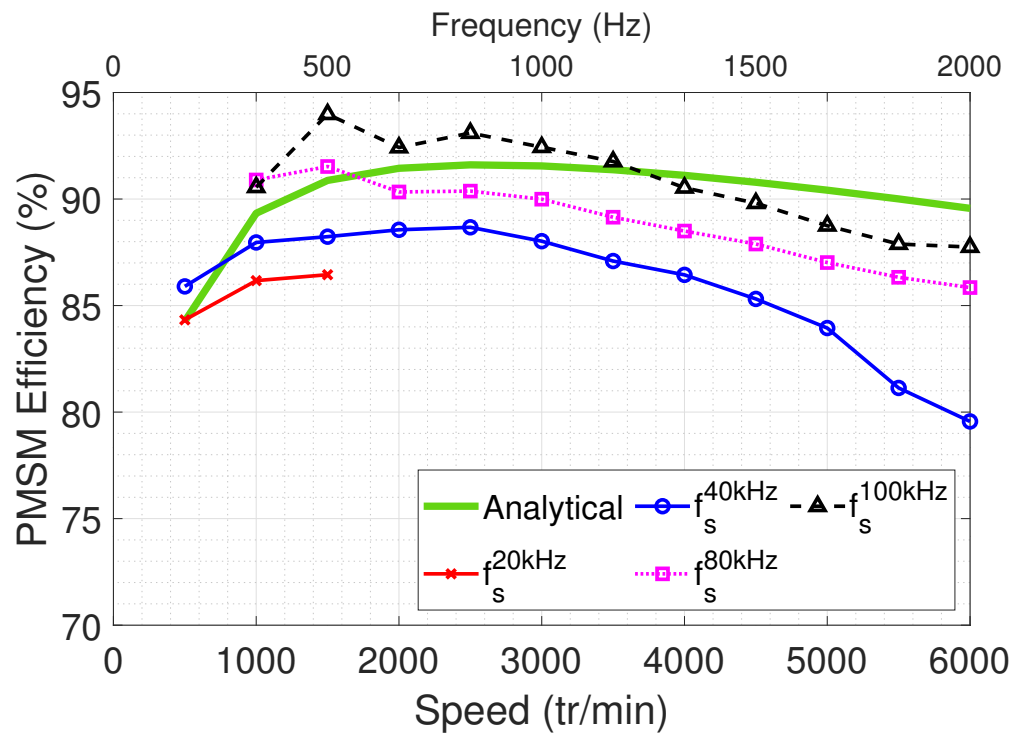


Figure 27. PMSM efficiency for different PWM frequencies.

Although increasing the switching frequency has beneficial effects on electrical machines, such as maintaining relatively constant torque, reducing losses, and increasing efficiency, it adversely affects converter efficiency. Figure 28 presents the experimental results conducted for inverter efficiency at different frequencies. These curves were derived from power measurements at the input and output of the inverter (SiC-MOSFET) during load tests (Figure 16). This finding implies the existence of an optimal switching frequency to maximize the efficiency of the conversion chain (inverter + motor), which may not necessarily be the highest frequency.

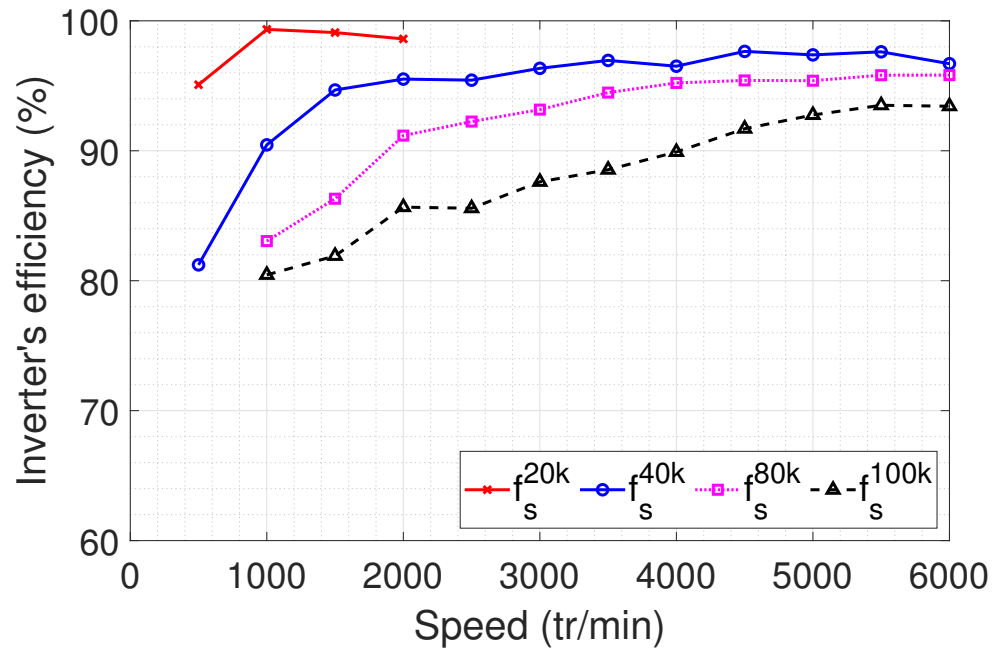


Figure 28. Efficiency of the PMSM for different PWM frequencies.

5.4. Overall Efficiency for PMSM and Inverter

Figure 29 illustrates the measurement results of the overall efficiency of the electromechanical conversion chain (inverter + motor) as a function of speed at full load. Measurements were conducted for four different PWM frequency values. The figure reveals that at low rotational speeds (below 1500 rpm), a PWM frequency of 20 kHz yields the highest efficiency. Between 1500 rpm and 4000 rpm, the optimal efficiency is achieved with a PWM frequency of 40 kHz. For speeds exceeding 4000 rpm, selecting a switching frequency of 80 kHz is preferable. Through curve interpolation, it becomes apparent that at very high rotational speeds (measurements were limited to 6000 rpm due to the DC bus voltage constraint), the efficiency curve decreases for a PWM frequency of 80 kHz, whereas it increases for a PWM frequency of 100 kHz. Thus, a PWM frequency of 100 kHz appears necessary to optimize efficiency. These findings underscore the importance of adjusting the PWM frequency according to the rotation speed to enhance the overall efficiency of the conversion chain.

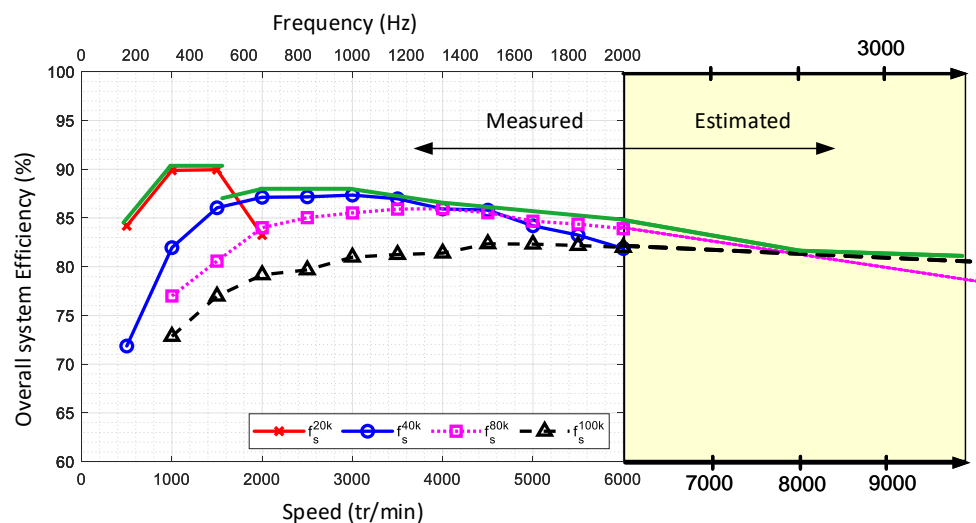


Figure 29. PMSM efficiency for different PWM frequencies.

## 6. Conclusions

The comprehensive investigation presented in this paper scrutinized the effects of high switching and fundamental frequencies on the parameters and efficiency of a PMSM drive. Through a combination of analytical studies, simulations, and experimental data, our findings conclusively demonstrate that enhancing the fundamental frequency, driven by the need for higher speed, decreases the efficiency of the PMSM and conversely increases that of the inverter. On the other hand, a high switching frequency leads to heightened efficiency in PMSMs and decreases that of the inverter. However, from the perspective of the entire system (inverter + PMSM), the total efficiency increases with the higher fundamental frequency. Nonetheless, the switching frequency of 80 kHz exhibits higher efficiency compared to 100 kHz for higher speeds. This improvement is primarily attributed to the diminished ripple in the machine's current, as confirmed by our analyses and empirical results.

**Author Contributions:** Methodology, P.P., E.J., T.L., L.B. and N.T.; Validation, P.P.; Investigation, P.P., E.J., T.L., L.B. and N.T.; Writing—original draft, E.J.; Writing—review & editing, P.P., T.L., L.B. and N.T.; Supervision, E.J., T.L. and N.T. All authors have read and agreed to the published version of the manuscript.

**Funding:** This research received no external funding.

**Data Availability Statement:** The original contributions presented in the study are included in the article, further inquiries can be directed to the corresponding authors.

**Conflicts of Interest:** The authors declare no conflicts of interest.

## References

1. Ehsani, M.; Singh, K.V.; Bansal, H.O.; Mehrjardi, R.T. State of the Art and Trends in Electric and Hybrid Electric Vehicles. *Proc. IEEE* **2021**, *109*, 967–984. [CrossRef]
2. Ritchie, H. Climate change and flying: What share of global CO<sub>2</sub> Emissions Come from Aviation? Our World in Data. Available online: <https://ourworldindata.org/co2-emissions-from-aviation> (accessed on 12 April 2021).
3. Sarlioglu, B.; Morris, C.T. More Electric Aircraft: Review, Challenges, and Opportunities for Commercial Transport Aircraft. *IEEE Trans. Transp. Electrification* **2015**, *1*, 54–64. [CrossRef]
4. Dalli, C.J.; Cilia, J.; Galea, M. Electro-Magnetic Design and Analysis for a High Performance, Aerospace Electrical Machine. In Proceedings of the 2023 26th International Conference on Electrical Machines and Systems (ICEMS), Zhuhai, China, 5–8 November 2023; pp. 2303–2308. [CrossRef]
5. Li, S.; Tong, W.; Wu, S.; Tang, R. Analytical Model for Maximum Mechanical Stress Calculation of High-Speed Interior Permanent Magnet Synchronous Motors with Modified Rotor. In Proceedings of the 2023 26th International Conference on Electrical Machines and Systems (ICEMS), Zhuhai, China, 5–8 November 2023; pp. 426–430. [CrossRef]
6. Liu, X.; Li, H.; Wu, Y.; Wang, L.; Yin, S. Dynamic Dead-Time Compensation Method Based on Switching Characteristics of the MOSFET for PMSM Drive System. *Electronics* **2023**, *12*, 4855. [CrossRef]
7. Hou, L.; Guo, Y.; Ba, X.; Lei, G.; Zhu, J. Efficiency Improvement of Permanent Magnet Synchronous Motors Using Model Predictive Control Considering Core Loss. *Energies* **2024**, *17*, 773. [CrossRef]
8. Yogal, N.; Lehrmann, C.; Henke, M. Permanent Magnet Eddy Current Loss Measurement at Higher Frequency and Temperature Effects under Ideal Sinusoidal and Non-Sinusoidal External Magnetic Fields. In Proceedings of the 2021 IEEE Energy Conversion Congress and Exposition (ECCE), Virtual, 10–14 October 2021; pp. 4176–4181. [CrossRef]
9. Xu, K.; Guo, Y.; Lei, G.; Zhu, J. Estimation of Iron Loss in Permanent Magnet Synchronous Motors Based on Particle Swarm Optimization and a Recurrent Neural Network. *Magnetism* **2023**, *3*, 327–342. [CrossRef]
10. Sirimanna, S.; Balachandran, T.; Haran, K. A Review on Magnet Loss Analysis, Validation, Design Considerations, and Reduction Strategies in Permanent Magnet Synchronous Motors. *Energies* **2022**, *15*, 6116. [CrossRef]
11. Wang, J.; Geng, W.; Li, Q.; Li, L.; Zhang, Z. A New Flux-Concentrating Rotor of Permanent Magnet Motor for Electric Vehicle Application. *IEEE Trans. Ind. Electron.* **2022**, *69*, 10882–10892. [CrossRef]
12. Lounthavong, V.; Sriwannarat, W.; Siritaratiwat, A.; Khunkitti, P. Optimal Stator Design of Doubly Salient Permanent Magnet Generator for Enhancing the Electromagnetic Performance. *Energies* **2019**, *12*, 3201. [CrossRef]
13. Yu, W.; Wu, Z.; Hua, W. Performance Evaluation of Stator/Rotor-PM Flux-Switching Machines and Interior Rotor-PM Machine for Hybrid Electric Vehicles. *World Electr. Veh. J.* **2023**, *14*, 139. [CrossRef]
14. Dorrell, D.G.; Hsieh, M.F.; Popescu, M.; Evans, L.; Staton, D.A.; Grout, V. A Review of the Design Issues and Techniques for Radial-Flux Brushless Surface and Internal Rare-Earth Permanent-Magnet Motors. *IEEE Trans. Ind. Electron.* **2011**, *58*, 3741–3757. [CrossRef]

15. Pellegrino, G.; Vagati, A.; Guglielmi, P.; Boazzo, B. Performance Comparison between Surface-Mounted and Interior PM Motor Drives for Electric Vehicle Application. *IEEE Trans. Ind. Electron.* **2012**, *59*, 803–811. [[CrossRef](#)]
16. Poolphaka, P.; Jamshidpour, E.; Takorabet, N.; Lubin, T. Performance Comparison between IGBT and SiC Devices in Three-Phase Inverter for High-Speed Motor Drive Applications. In Proceedings of the 2022 25th International Conference on Electrical Machines and Systems (ICEMS), Chiang Mai, Thailand, 29 November–2 December 2022; pp. 1–6. [[CrossRef](#)]
17. Poolphaka, P.; Jamshidpour, E.; Lubin, T.; Baghli, L.; Takorabet, N. Comparative Study of IGBT and SiC MOSFET Three-Phase Inverter: Impact of Parasitic Capacitance on the Output Voltage Distortion. *Actuators* **2023**, *12*, 355. [[CrossRef](#)]
18. Tolstoy, G.; Ranstad, P.; Colmenares, J.; Peftitsis, D.; Giezendanner, F.; Rabkowski, J.; Nee, H.-P. An experimental analysis on how the dead-time of SiC BJT and SiC MOSFET impacts the losses in a high-frequency resonant converter. In Proceedings of the 2014 16th European Conference on Power Electronics and Applications, Lappeenranta, Finland, 26–28 August 2014; pp. 1–10. [[CrossRef](#)]
19. Qureshi, M.S.; Kerai, A.A.; Fatima, S.A.; Shah, S.J.; Khan, K.A.; Ali, A.; Maheshwari, L.; Makda, I.; Usman, A. Effects of Parasitic Elements in High Frequency GaN-based DC-DC Converters for Electric Vehicle Applications. In Proceedings of the 2023 25th International Multitopic Conference (INMIC), Lahore, Pakistan, 17–18 November 2023; pp. 1–6. [[CrossRef](#)]
20. Pyrhonen, J.; Jokinen, T.; Hrabovcova, V. *Design of Rotating Electrical Machines*; John Wiley & Sons: Hoboken, NJ, USA, 2013.
21. Steinmetz, C.P. On the law of hysteresis. *Proc. IEEE* **1984**, *72*, 197–221. [[CrossRef](#)]
22. Baghli, L.; Jamshidpour, E. Implementing a 200 kHz PWM Field Oriented Control using RTLib and C program on a dSPACE MicroLabBox. In Proceedings of the 2022 2nd International Conference on Advanced Electrical Engineering (ICAEE), Constantine, Algeriam, 29–31 October 2022; pp. 1–6. [[CrossRef](#)]

**Disclaimer/Publisher’s Note:** The statements, opinions and data contained in all publications are solely those of the individual author(s) and contributor(s) and not of MDPI and/or the editor(s). MDPI and/or the editor(s) disclaim responsibility for any injury to people or property resulting from any ideas, methods, instructions or products referred to in the content.